Chapter 5

HyDRa: Vortex Polishing with a Deterministic Hydrodynamic Radial Polishing Tool

Erika Sohn, Esteban Luna, Elfego Ruiz, Luis Salas and Joel Herrera

Additional information is available at the end of the chapter

http://dx.doi.org/10.5772/intechopen.75524

Abstract

This work presents the deterministic hydrodynamic polishing system (HyDRa (HyDRa-dynamic Radial Polishing Tool) based on a polishing tool developed at the Instituto de Astronomía, UNAM. HyDRa is one of several modern deterministic polishing techniques that allow for computer controlled finishing of complex optical surfaces. The HyDRa system is based on a hydrodynamic polishing tool that generates a variable-density abrasive flow that makes possible the production of high-quality optical surfaces of diverse materials. The tool comprises several stacked operational stages that generate a grazwing abrasive flow with a predictable, zero-force erosion footprint on the workpiece that removes material. A recent innovation to the hydrodynamic polishing tool adds a switching capacity to the tool that allows the polishing action to be interrupted at will, without losing the stability of the operating parameters. This further increases the versatility and performance of the tool, since it is now possible to polish only the areas where the surface needs correction. Pulsed polishing also adds several techniques to this polishing method that further increase the system's versatility.

Keywords: deterministic polishing, fluid jet polishing, vortex polishing, pulsed polishing, simultaneous polishing with multiple tools

1. Introduction

As the demand to fabricate larger and increasingly complex aspheric optics becomes more common, the need for deterministic polishing tools which can meet these demands has motivated the development of the hydrodynamic, polishing tool (HyDRa).

The HyDRa polishing tool [1, 2] is a non-contact, zero-force hydrodynamic tool that rotationally accelerates a slurry and air mixture and expels it tangentially onto the workpiece. It consists of several operational stages: an abrasive suspension (water and polishing grit) is fed to the tool's first operational stage, where it is mixed with air at a controlled pressure in order to produce a variable-density abrasive foam. This foam then enters the rotational acceleration chamber, where it is sped up to high revolutions per minute (RPM). The rotational energy of the flow then turns into radial velocity in a nozzle that forms between the tool's divergent output and the workpiece. In this way, the abrasive particles graze the workpiece in closely tangential trajectories. Thus, the polishing particles generate a shearing action that removes material in a ductile removal process, as described in [3]. The drag generated by this radial flow forms a central low-pressure zone (vacuum) surrounded by a high-pressure ring. As a result, the tool floats over the workpiece, exerting no net force onto it [4], since these regions cancel each other out. This poses many advantages in modern deterministic polishing, in particular the capability of polishing ultra-thin surfaces, such as semiconductor wafers and optical membranes.

The HyDRa tool belongs to the fluid jet polishing (FJP) family, originally developed by Fähnle et al. [5]. Although HyDRa also expels an abrasive suspension onto the surface to be polished, there are several basic operational principles that differ from the classic FJP technique. The FJP method, and most other polishing techniques, needs to apply pressure onto the workpiece, in order to remove material. In some cases, as in the classic FJP technique, the force that is exerted onto the material can be minimized by using a small contact area; see for example [6], where the force on the workpiece is less than 1 N. This however, could represent a trade-off between footprint size and removal rate; removal rates of <0.01 mm^3/h are common for 1–2 μm Cerium oxide polisher [6]. Other deterministic methods, such as ion beam figuring (IBF), are non-contact, zero-force processes that present removal rates of up to 50 mm^3/min [7] without degrading the initial micro-roughness.

2. Polishing with HyDRa

This section describes the generalities of polishing with the HyDRa system. A typical static removal footprint is shown in **Figure 1**.

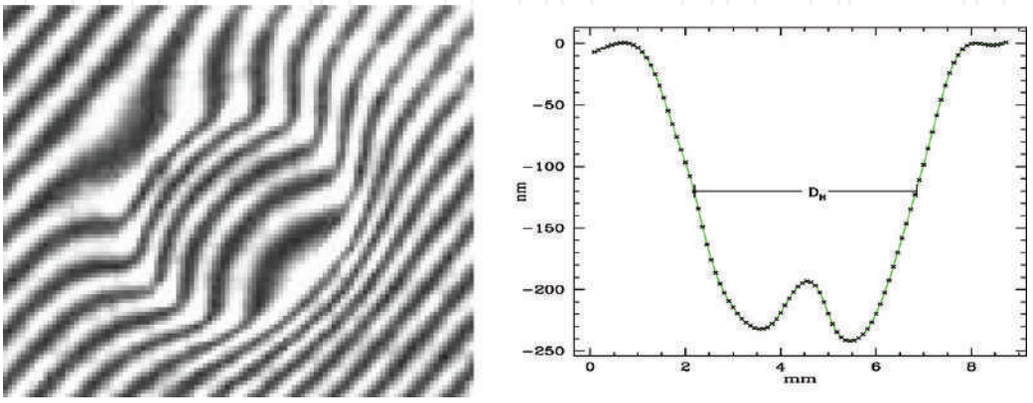

Figure 1. Tool influence function. The image to the right shows the removal function profile extracted from the interferogram to the left. This profile was obtained by operating the tool for 2 s on a fixed position over the workpiece. D_H is the full width at half maximum (FWHM) of the removal function. Tool footprint diameters typically range between 3 and 10 mm, depending on the particular tool.

http://dx.doi.org/10.5772/intechopen.75524

As can be seen, the removal takes place in a ~5 mm diameter region that has an M-shaped geometry. Removal in the central region is about 20% lower than the peripheral region. Removal is a function of slurry density (ρ) and accelerating air pressure (P_T), slurry flow, i.e., flow rate (F_1), and is a linear function of dwell-time. In order to attain deterministic polishing, all tool parameters are controlled with high precision, as described in Section 4.

2.1. The HyDRa polishing rig

The HyDRa tool is part of a complex polishing robot, consisting of a CNC positioning device; a fluid and compressed air control system; a slurry management unit, which stirs the slurry and controls its density; and a software package that obtains error maps from a series of interferometers, and generates dwell-time/constant-velocity PWM trajectories. These trajectories correct the workpiece figure, depending on the selected method (pulsed or continuous operation), as the block-diagram of **Figure 2** illustrates.

The HyDRa tool is attached to a five degree of freedom (DOF) polishing machine with force feedback, based on a 2.4 × 2.4 m Cartesian CNC, with two additional DOF (tip and tilt), implemented by means of a 3-actuator hexapod. This configuration allows the generation and polishing of any surface geometry. Since feedback control keeps all polishing parameters constant, removal is exclusively a function of dwell-time. In this way, figure correction depends on the trajectory followed by the tool and the velocity at each point along it, which requires that the CNC be capable of following five-dimensional, controlled-velocity trajectories. Simultaneously, z-axis movement is controlled so that the tool can accurately follow the surface contour with zero-force. Although the machine's repeatability is around 10 μm, the removal is accomplished with nanometric accuracy due to a load cell that regulates tool height over the workpiece, as reported in [4]. The slurry conditioning unit (SCU) supplies a

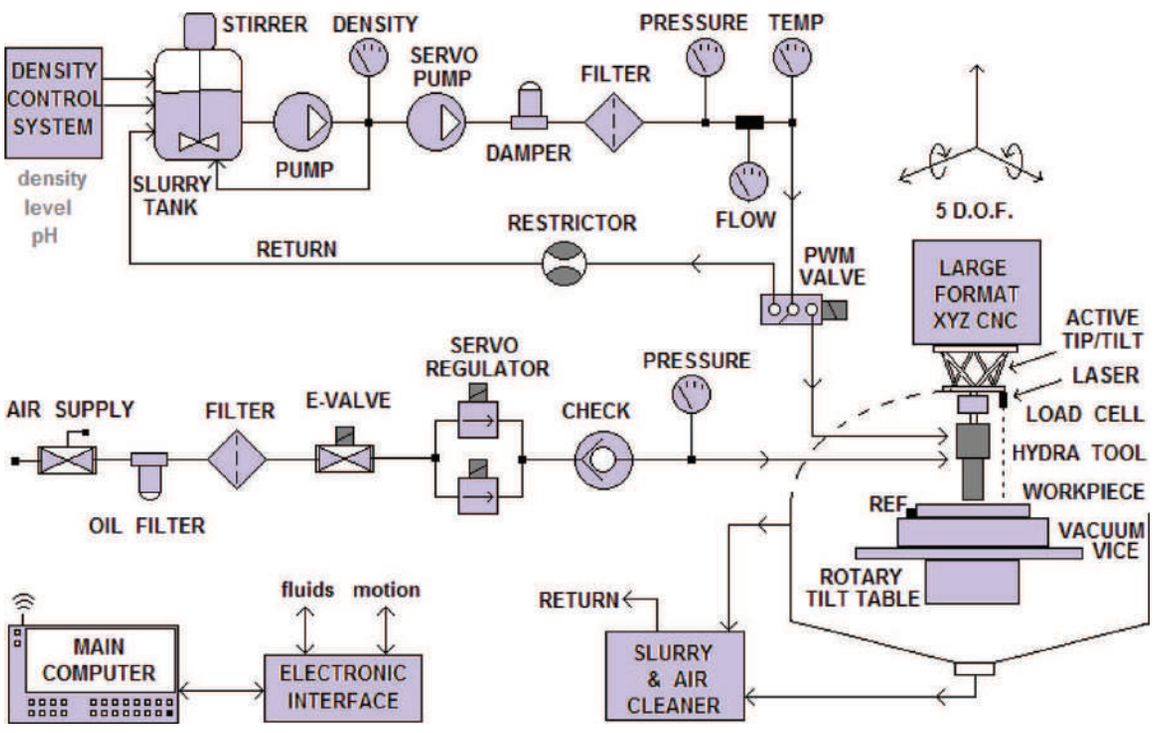

Figure 2. HyDRa polishing process setup, (see text).

density controlled polishing suspension to the HyDRa slurry supply system. It also captures and reincorporates the liquid and atomized slurry that is expelled from the tool. The density is continuously monitored by means of a photodensitometer and controlled by means of polishing-paste and water supply systems. The expelled slurry is captured by the return system, which consists of a blower that reincorporates this slurry and air into the SCU container, forcing the mixture through a washed-air system.

A pump is continually recirculating the polisher in the container, and a derivation supplies filtered slurry to the HyDRa slurry control system. The slurry that flows into the tool is fed by means of a damped-diaphragm DC pump that is feedback-controlled by means of either a flow meter or a pressure sensor. In order to reduce air contamination, the HyDRa system polishes in shallow immersion so that an air-lock for the return system is formed. The HyDRa tool accelerates an abrasive foam, composed of a variable-density suspension of slurry and air created by means of an air control system that regulates the foaming and propelling air pressures using electromechanic air regulators, pressure sensors and control electronics. All polishing parameters are acquired with a data acquisition card, and controlled and visualized in LabView®. The surface is fixed onto the CNC platform as the tool is swept over the surface in a pattern chosen by the user. Pulsed operation of the tool sweeps the tool(s) along the workpiece at a constant velocity, switching the polishing action on and off depending on how much material needs to be removed. The slurry is fed to the tool at controlled pressures and flow rates. The tool is supplied with compressed air to operate the foaming and acceleration stages. The abrasive foam is radially expelled through the tool nozzle onto the surface to be polished, as described above. Tool height is controlled by the feedback variable provided by the load cell, so that the CNC can adjust tool height in order to polish with zero force, as is discussed below.

2.2. Zero-force polishing

One of the central advantages of the HyDRa tool resides in that it can be adjusted to exert zero force on the work surface, while maintaining considerable removal rates (~10 mm^3/h). The flotation effect is described in more depth in this section.

As the HyDRa tool expels the slurry through its nozzle, the rotational energy of the flow is converted to radial velocity. The drag generated by this radial flow produces a central low-pressure zone that is surrounded by a vortex which is in turn confined by a ring shaped, positive thrust zone. This effect differs from the linear jet polishing technique [3, 8] in that, in normal-incidence, classic jets, the pressure profile is represented by a Gaussian distribution, where the maximum is located at the jet's center. In contrast, the pressure distribution of HyDRa on the workpiece presents negative values at the footprint's center and is circumscribed by an annular, positive-pressure region. With this, the force on the workpiece can be adjusted to net zero-force. In **Figure 3a**, footprint pressure vs. distance from the center of the tool is plotted. This was obtained by means of a 0.46 mm diameter orifice connected to a pressure sensor over which the tool footprint was radially scanned. As can be seen, a low pressure zone forms at the central part of the footprint and, as the radius increases, the gauge pressure increases to a maximum. It then falls again as the orifice approaches the tool's outer radius.

http://dx.doi.org/10.5772/intechopen.75524

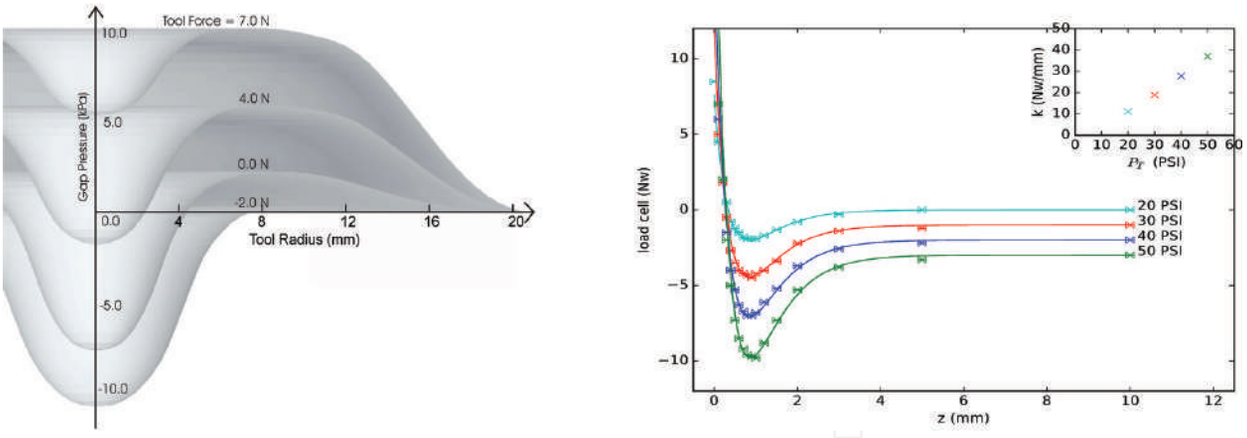

Figure 3. (a) (left) Pressure distribution as a function of tool radius for different operating pressures. (b) (right) Force applied by the HyDRa tool as a function of distance Z from the work surface for accelerating pressures P_T = 20, 30, 40 and 50 PSI. For clarity, a constant offset has been added to the 30, 40 and 50 cases. Typical error bars are 0.1 N for the load cell and 20 μm for the Z position. The solid lines are an analytical function fit derived from a Morse potential. In the upper right inset, the restitution spring constant is shown to be related to P_T. When an external holding force F_h is applied to the tool and pushes it against the workpiece, the vacuum force F_v has a tendency to decrease as the thrust force F_e is increased.

As the tool moves away from the workpiece, the vacuum has a tendency to increase, as the thrust force tends to decrease; in consequence, the balance of these two forces is a function of the tool's distance from the surface to be polished. With this, several operational modes can be achieved, one of them allowing the tool to freely float over the surface without the need to rigidly attach it to a positioning device. In this case, the tool's weight is counterbalanced by the thrust and vacuum forces. When the HyDRa tool is mounted onto a passive hexapod through a load cell, the support force F_h counterbalances the tool weight mg and the remaining forces to zero, while maintaining the tool in a static position.

The load cell value F_h is then used as feedback for the control system to maintain zero force on the workpiece. This is done by adjusting the z-axis of the CNC/hexapod.

We measured the tool and workpiece force interactions as a function of separation. In **Figure 3b**, the overall behavior of this interaction is shown in experiments where slurry accelerating pressures of 20 to 50 PSI and a polishing slurry flow of 5 ml/s were used. The distance over the workpiece was modified from several millimeters, down to a few hundred microns. The values of the load cell F_h were used to obtain the substrate force F_x, as explained above.

When the tool exceeds a certain distance, the workpiece experiences no force (see **Figure 3**). As the tool approaches the substrate, a negative force (attraction) is produced by a vacuum that develops between the workpiece and the HyDRa tool. As the tool further approaches the workpiece, a positive repulsion force is experienced, caused by the thrust force. At a few hundred μm from the workpiece, the vacuum and thrust forces balance each other out to zero. Here the surface can be polished without being deformed by the tool.

The combination of attractive and repulsive forces commonly arises in physical problems. One of such is given by the empirical Morse potential of diatomic molecules $U(z) = B\left(1 - e^{(-\alpha(z-z_m))}\right)^2 - B$, where B is the dissociation potential and z_m is the separation at which the minimum of the potential is

P_T (PSI)	B (N mm)	α (1/mm)	z_m (mm)	k (N/mm)
50	10	1.36	0.36	40
40	7.5	1.36	0.34	27.7
30	5.1	1.36	0.34	18.9
20	3	1.36	0.34	11.1

Table 1. Fitting curve parameters.

reached, which constitutes a stable equilibrium separation. A force can be readily obtained from this potential by calculating its gradient: $F(z) = -\frac{d}{dz}U(z)$. We have plotted this force along the data of the figure by least-squares fitting the three parameters, B, α and z_m; their resulting values are listed in **Table 1**. A reasonable fit is obtained, and some insights may be derived from this exercise. It can be noted that, as the accelerating pressure P_T increases, so does the depth of the potential well and thus the amplitude of the forces involved, as given by the parameter B. However, the minimum of the potential is found roughly at a constant separation z_m of around 340 μm. At this distance, the force derived from the potential is zero (since the derivative of the potential is zero) and the tool floats over the work surface in stable equilibrium. If we approximate the minimum of the potential by a square law (Hooke's law) a restitution spring constant $k = 2\alpha B$ can be obtained, which measures the force with which the stable position is restituted. The values of k are also given in **Table 1**. As indicated in the inset in **Figure 3b**, k is a linear function of the accelerating pressure P_T.

2.3. Tool influence function and removal rates

Several tools have been developed to accommodate for different removal rates that range from 1 to 600 mm^3/h. This section presents measurements of static and volumetric removal rates for a medium removal-rate tool with a nozzle diameter of 3.8 mm. Several polisher grits have been tested: Cerium oxide (Opaline) with a particle size of 1 μm, and aluminum oxide (μ-grit) with particle sizes of 5 and 12 μm, suspended in water at a constant relative density of 1.09. Samples of different materials were polished: standard window glass, water-free fused silica (Infrasil®-302), BK-7 borosilicate, and Ohara's CLEARCERAM-Z® vitroceramic.

The measurements were performed by scan-sliding the tool over the sample at a constant speed and a corresponding zero-force tool height. The resulting cavity was measured interferometrically, and both the volume of removed material and the depth of the cavity were calculated. With these measurements the static removal rate D_S (depth/time) and the volumetric removal rate D_V were then calculated. We performed these measurements at different operational conditions of accelerating pressure (P_T) and slurry flow (f_p). In all cases, the relative density of the slurry was kept at 1.09. In **Figure 4**, the test results are shown. In all three panels, the left vertical axis D_V is related to D_S as $D_V = D_S * A$, where A is the tool footprint area. Each plot indicates the dependence of removal on the accelerating pressure P_T. The top left panel, where Cerium oxide was used, slurry flow f_p values of 3, 5 and 7 ml/s on window glass were tested. These are indicated as numbers on the curve.

http://dx.doi.org/10.5772/intechopen.75524

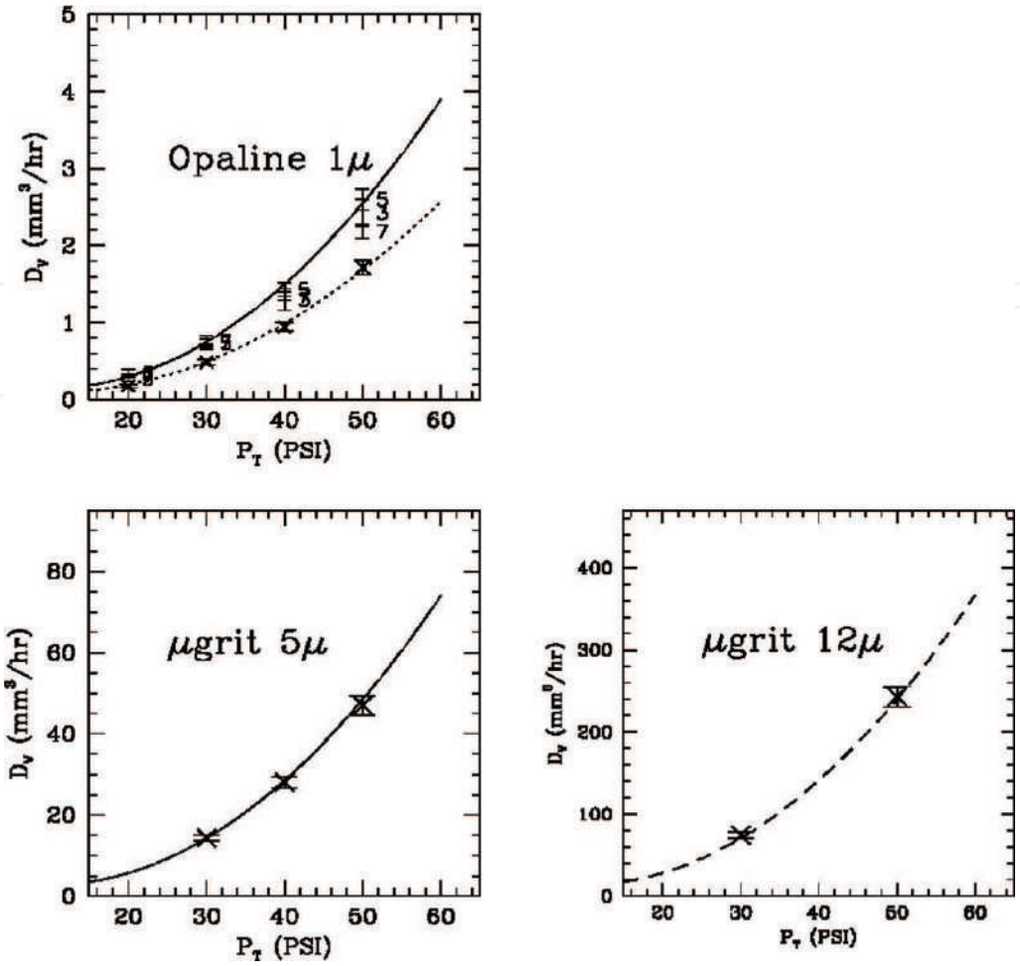

Figure 4. Volumetric removal rate D_V as a function of accelerating pressure (P_T) for various polisher types: 1 μm cerium oxide (Opaline), 5 μm aluminum oxide (μgrit) and 12 μm aluminum oxide. Opaline removal rates are presented for window glass (solid line), fused silica, and borosilicate (dotted line). Removal of μ-grit is shown for window glass and CLEARCERAM®-Z vitroceramic. All fitted curves are versions of the same second order polynomial law, scaled by a factor that is a function of substrate material and particle size (see text). Zero-force polishing was achieved at the corresponding tool height for this effect.

As can be noted, the highest removal rate for this tool is achieved with a slurry flow of 5 ml/s, thus this flow was employed for all consecutive experiments. Removal rates up to 2.5 mm^3/h at 50 PSI are obtained for this polisher. The $f_p = 5$ points are well fitted by a second order polynomial. In the first panel we also show the results of polishing a fused silica sample (crosses). In this case the hardness of the material causes the removal rate to decrease to 66% compared to window glass. The dotted line that fits these values is obtained by multiplying the same D_S polynomial by a small factor. In the lower left panel we tested the removal rate of 5 μm aluminum oxide grit on glass (crosses). The volumetric removal rate rises to ~50 mm^3/h at an accelerating pressure of 50 PSI. The solid line is the D_S polynomial obtained previously, multiplied by 19. Again, a very good fit can be seen. Lastly, in the lower-right panel, the removal rate of aluminum oxide grit (12 μm particle size) on Ohara CLEARCERAM® vitroceramic is shown. Removal was so large that it was impossible to measure it reliably with an interferometer, so the resulting cavity was measured by means of a needle profilometer. Only two points were

taken in this experiment (crosses in the last graph). If the same polynomial D_S were to be fitted (dashed line), it would have to be multiplied by 94. For all cases, the removed volume per abrasive particle is 3 to 5 orders of magnitude lower than the particle's volume. The kinetic energy as well as the grazing incidence associated with both the cerium and alumina particles, creates stresses that are not large enough to produce permanent dents. Resulting typical micro-roughnesses of 2, 24, and 31 nm, for grit sizes of 1, 5, and 12 μm, respectively, are around three orders of magnitude smaller than the particle sizes. These tests demonstrate that independently of grit size and material, as well as substrate hardness, behavior of removal as a function of accelerating tool pressure is comparable, which indicates that the same material removal process discussed above is taking place. The scaling parameter is an indicator of how efficiently a particular abrasive removes material from a surface of a given hardness. All HyDRa tools present this same relationship of removal as a function of P_T and grit size for pressures of up to 90 PSI. Currently, typical removal rates of ~15 mm^3/h @ 90 PSI, using 1 μm Opaline on borosilicate glass, are common.

2.4. Software

The HyDRa trajectory planning tool (HyTPT) is a software package developed specifically for the HyDRa tool [9]. It feeds machining code to a CNC or any computer-controlled positioning device, based on the error map that has been obtained interferometrically. When only one HyDRa tool is available, the amount of material that is removed at each specific position is proportional to the dwell time. This dwell time can be controlled either by the speed of the tool along a given trajectory when the tool is operated in continuous mode, or by the width of the pulses when operated in pulsed mode.

In HyTPT (**Figure 5**) a main window presents the project name and grants the user the ability to go from error maps to machine coordinates in four steps:

1. **Error Map alignment:** This allows the easy alignment of the error map, and the determination of its center, orientation and pixel size. The basic shapes are rectangular, circular, and annular surfaces.
2. **Base trajector:** It is possible to select the base trajectory from a series of curves: from simple raster patterns to more complex curves, such as trochoids and rotating triangles. It is possible to define and analyze each curve from the point of view of trajectory density, total polishing time, and speed at each point, among several others.
3. **Surface shape:** The shape of the surface, currently any on- or off-axis conic section, is defined in this window. The 2-D base trajectory is projected onto this 3-D surface. In addition to the 3-D trajectory the normal vector to the surface at each position is calculated, so that the CNC may orient the HyDRa tool normal to the surface along the trajectory.
4. **Machine coordinates:** A set of alignment tools facilitates the transformation of surface coordinates to machine coordinates. These routines communicate with the CNC machine and are developed for each particular CNC or robot arm to which the HyDRa tool is attached.

http://dx.doi.org/10.5772/intechopen.75524

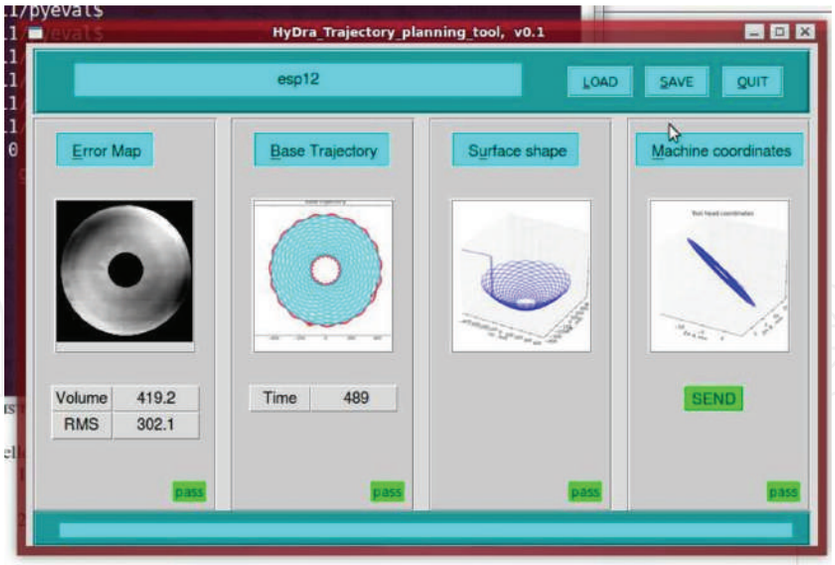

Figure 5. HyTPT software main interface showing all four steps.

Finally, the centering and orientation parameters, nine in total, are determined in order to properly align the system. Once each of these parameters has been calculated, the trajectory is delivered to the CNC machine, or robot arm so it can be executed there.

3. Pulsed polishing

Due to its hydrodynamic properties, the original HyDRa tool [1] does not allow the modification or switching of any of its operational parameters during operation. Therefore, in order to control the removal, dwell time is modified by means of tool velocity. However, there is a maximum tool velocity imposed by CNC limitations, that fixes a minimum, non-zero amount of material that can be removed with the tool. This poses problems for several operational applications, such as zonal corrections, multi-head or tessellated polishing, and edge problems. A new HyDRa tool design (patent pending) [2] overcomes these problems, by switching one of the operational parameters (polisher flow). This enables the pulsing of the abrasive action at will, without affecting tool bias. The ability to operate the HyDRa tool in a switched manner widens its overall performance and efficiency, adding new applications. It is not simple to switch most of the tool's operational parameters during use, since this causes a loss of tool bias, which affects the flotation capability. Restoring these parameters on the fly takes time and produces unwanted effects such as cavitation. This has limited the polishing strategy to making full sweeps of the entire surface. When needing to polish only a small section, the region must be approached with the tool biased, leaving behind an unwanted track and approach and exit marks. A new HyDRa tool design has been developed which allows switching slurry flow without losing tool bias. Switching frequencies of up to 10 Hz, and pulses as narrow as 10 ms, can be achieved with this new tool. This is accomplished by means

of an overdriven electro-valve which is installed in, or close to, the tool. This allows the use of polishing pulses that can be applied on a per-pixel basis or in a continuous scan using pulse width modulation (PWM) techniques. With this feature, dwell time can be controlled below the minimum attainable by a continuous action at the maximum CNC speed.

3.1. Linearity

A pulsed HyDRa tool with a 7 mm footprint has been developed and tested for linearity. **Figure 6a** shows the results of erosion vs. dwell-time. Pulse width was varied at constant increments, starting from 10 ms to a maximum of 500 ms, as the tool was moved at 0.2 mm increments, overlapping 35 times at each tool footprint diameter. The erosion was measured using a Fizeau interferometer and the result was normalized, so that removal corresponded to a single pass of the tool over each point along the line that was polished. Error bars are primarily due to errors produced by the subtraction of the base reference during interferogram reduction. A removal resolution of 0.1 nm/ms can be seen from the data. Noticeable polishing effects were observed at 25 ms. We attribute this effect to the electro-valve response time, which can be improved by using faster actuators.

3.2. Pulsing the polishing process

3.2.1. Pulse width modulation polishing (PWM)

It is now possible to control the duration of a pulse as a fraction of the time it takes the tool to travel a distance of one footprint diameter.

The depth of removed material for a raster scan pattern h, can be given by:

$$h = D_V Y / VS$$

where D_V is the volumetric removal rate, Y is the PWM duty cycle (ON time divided by the period T), V is the CNC velocity, and S is the raster step size. The period of the switching

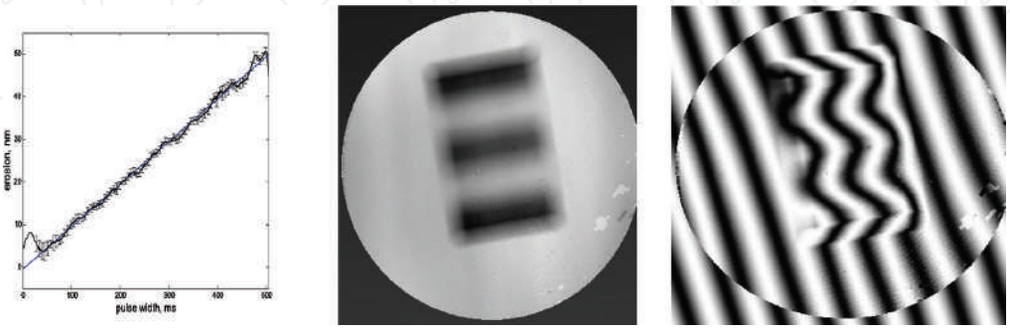

Figure 6. (a) Erosion vs. pulse-width in a linearity test. (b) Response function of the tool for pulsed operation at constant tool velocity. The tool was switched in a PWM mode, with a 50% duty cycle and 100 ms on/off switching times. The raster pattern used to generate this surface is perpendicular to the surface produced in the figure. Pixel size is limited by footprint size. Tool velocity was chosen so the pulses could be resolved independently.

signal is $T = D/V$, where D is the tool footprint diameter. In the time it takes to cross a tool footprint, there is a single pulse whose width can be varied from zero to the entire footprint diameter. The depth of the removed material $h = \beta\tau$ is proportional to the dwell time τ, defined by $\tau = \Upsilon D/V$, with a proportionality constant $\beta = D_V/SD$. When $\Upsilon = 1$, which is the continuous mode, tool removal (dwell time) h is controlled by CNC velocity. When $\Upsilon < 1$, which is the pulsed mode, h is controlled by means of switching the slurry supply and keeping the tool velocity constant. The continuous mode is limited to removals greater than $h_{\{min\}} = D_V\,\Upsilon/V_{\{max\}}S$. In order to obtain a lower removal, the pulsed mode must be employed.

For a tool footprint diameter of 7 mm and a maximum CNC velocity of 2000 mm/min, the minimum period of the switching signal will be 0.2 seg, or 5 HZ, which is within the 10 Hz switching frequency range. In an extreme case, where the duty cycle is switched between 0 and 1 while maintaining a constant velocity, it is possible to create a pixelated pattern that is useful for determining the response function of the pulsed tool (**Figure 6b**). A fringed pattern can be observed where the interface between the regions presents a slope that corresponds to the tool footprint diameter, which is the limiting polishing element size (*poxel*, or polishing element).

3.2.2. Zonal polishing

When only a small section of the surface needs to be polished, this region must be approached with the tool turned on, leaving behind unwanted tracks, as well as approach and exit marks. This is solved by using the pulsed mode of the HyDRa tool. When an isolated region that needs further polishing is identified, a dampening band of constant width surrounding it is defined. Assuming a raster pattern is used, the region is approached with the HyDRa tool fully operational with $\Upsilon = 0$, until it enters the dampening region. Here velocity is smoothly incremented to the value needed inside the region while at the same time, the desired dwell time is controlled by means of PWM. The width of the dampening region is determined by the CNC acceleration and deceleration capabilities. Inside the region to be corrected, either a pulsed or continuous polishing can be used in order to maximize efficiency.

3.2.3. Pixel polishing

In the constant velocity PWM polishing case, the resulting response function in the sweep direction is different from the response function of the transverse, raster direction. When a symmetrical finishing is needed, it is possible to employ the pixel polishing method, which consists of stepping the tool at discrete positions with respect to each other, covering the region of interest with the same step increments in both axes. The tool is then switched on for the necessary time in order to achieve the desired removal for each position. This method can also be useful when very localized zonal polishing is needed. This allows the tool to either follow a raster pattern, or any other trajectory or set of discrete positions over the region of interest. An example of this method was used in Section 3.1 for the linearity test, where it was shown that a removal resolution of 0.1 nm can be attained.

3.2.4. Tessellated polishing

In the polishing of meter-class surfaces, efficiency is limited due to HyDRa's small footprint size and volumetric removal rate. Efficiency, however, can be improved by simultaneously polishing the surface with several HyDRa tools. These tools can be mounted on independent polishing robots, where each robot tackles a certain section of the surface. Alternatively, several tools can be mounted on a single robot arm, as described below. This method poses several problems, such as obtaining smooth seams between sections, approaching each section without leaving marks, and avoiding collisions as two tools concurrently approach the boundary between sections. In order to obtain a seamless interface between two independent sections, it is necessary to approach the boundary following special trajectories, such as the wedge pattern shown in **Figure 7** (bottom). This trajectory avoids duplicating dwell time at the seam, such as would happen if a rectangular pattern were used (top of **Figure 7**).

3.2.5. Polishing run interrupt

When the polishing process needs to be interrupted, it is now possible to stop at any point on the surface and continue polishing at a later time.

3.2.6. Edge problem

As in other polishing methods, the HyDRa tool tends to leave a small (one footprint diameter) fallen edge. In order to overcome this with the unmodified HyDRa tool, tool velocity is

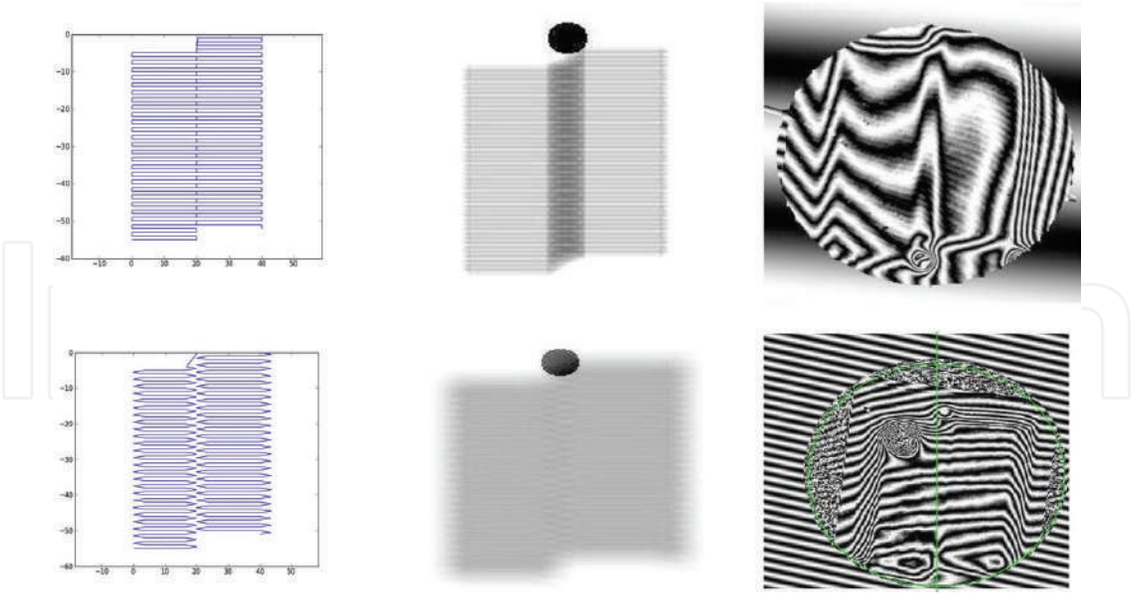

Figure 7. Tessellated polishing showing two different trajectory approaches. The figures to the left show the region of the interface between two raster patterns that use a rectangular (upper) and wedge (lower) seam at the boundary. The middle figures show a simulation of the resulting removal with the tool moving at a constant velocity and without PWM. Note the approach/exit tool mark at the beginning/end of the trajectory due to not switching the tool off. The interferograms to the right are actual polishing experiments. As can be seen, the raster pattern using rectangular trajectories duplicates removal at the seam, whereas the wedge trajectory produces a seamless interface. Another possible solution is to vary the pulse width at the seam, in order to match the dwell time between adjacent polishing sections.

http://dx.doi.org/10.5772/intechopen.75524

incremented as the tool approaches the edge, reducing dwell-time. This is counterintuitive and can present CNC control problems, since the tool is accelerated in a region where it should be preparing for a raster direction change. The on–off capability of the new tool can alleviate this problem, since dwell-time can be controlled without having to increment tool velocity at the edge region. In fact, this method allows for decelerating the CNC in order to prepare for a direction change.

3.2.7. Convergence

Another advantage of being able to pulse the tool is a quicker convergence towards the desired surface [10]. As pointed out in [11], the existence of a minimum amount that will be removed due to not being able to turn the tool off (h_{min}), limits the amount of material that can be removed in each run, whereas, by being able to pulse the tool, h_{min} can be made zero, allowing for a maximum value of f, further increasing the polishing convergence rate.

3.3. Multiple-head polishing

Since HyDRa tools can now be pulsed, several polishing heads can be mounted onto a common arm which moves at a constant velocity over the surface. Dwell time is then controlled using PWM for each tool, as required by the error map. We can also take advantage of the self-conforming capabilities of HyDRa, in that it is not necessary to employ a positioning device to conform the parallelism of the tool to the surface. Only one degree of freedom (DOF) per tool is required. Each loop is closed with a load cell signal and implemented by means of a linear stage, which permits zero-force polishing while freely following the local sag and tilt of the surface. Another advantage of this type of polishing is that one single slurry supply system can be used for all the tools, simplifying the system and considerably reducing the costs. Polishing efficiency becomes a function of the number of tools, and in the case of a matrix configuration, several polishing runs can be implemented into a single sweep, reducing polishing time.

By polishing with several tools, each tool is essentially given a section of the surface and the boundaries between sections are finished seamlessly, either by employing wedged joints, or by using PWM. Among the possible multi-tool configurations are matrix, linear and spiral layouts:

3.3.1. Linear

By mounting several HyDRa tools onto a single polishing arm, attached to a Cartesian CNC machine, it is possible to cover an area by sweeping the arm in the x and y directions. Each tool is separated from the next by a fixed distance δ in the x axis. The sweeping action in the x axis is done by moving the arm by δ, and then advancing with the selected raster step in the y axis. The overlap between the sections assigned to each tool is managed by either using tessellated or the PWM techniques, as described above. There are certain considerations to be taken into account for this method, particularly due to the edge problem that arises when polishing circular or non-rectangular surfaces. There will always be a tool that needs to either enter or exit the surface, while others are already polishing. Additionally, since these tools need to take advantage of their self-conforming capability, as they approach the edge of the workpiece, they loose floatability. These problems can be dealt with by adequate trajectory programming.

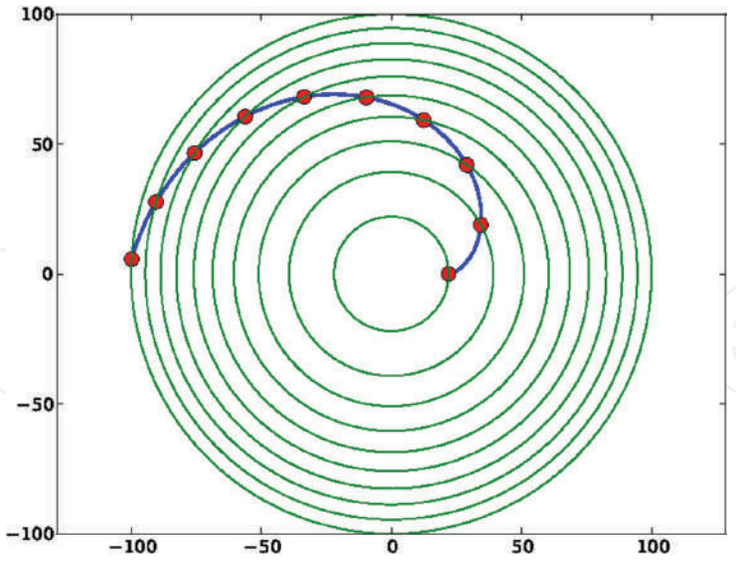

Figure 8. Hydra tools mounted on a spiral arm (see text).

3.3.2. Matrix

The linear configuration can be expanded by creating a matrix of tightly packed HyDRa tools maximizing tool number in order to minimize polishing time. The working principle is the same as the linear case, but adding *M* rows. This is equivalent to carrying out M polishing runs in a single iteration.

3.3.3. Spiral

In the case of large circular mirrors, it may be more efficient to polish the mirror by placing it on a rotary table. If we seek to fix as many HyDRa tools as possible onto a single arm, two conditions must be met. First, the number of tools should increase as r^2, so that each tool covers the same mirror area. Secondly, tools must be packed at the maximum allowable density, so that each tool sits next to the following one. Therefore, the shape of the arm must be a kind of spiral which is possible to solve for. By calculus of variations a spiral curve parameterized by the (increasing) radial coordinate, given in polar coordinates (r, θ) results in: $\theta(r) = \sqrt{4k^2 - 1/r^2} - \arctan\left(\sqrt{4(kr)^2 - 1}\right), r > 1/2k$. An example of this is shown in **Figure 8**, where HyDRa tools are mounted at equal separations along a spiral arm and may move along it to span equal areas, as the surface under it rotates.

4. Polishing parameters

Of the multiple finishing techniques currently in use, the ones based on sub-aperture polishing may be candidates for deterministic polishing, provided that the uncertainty of key polishing parameters is minimized. Deterministic polishing relies on a stable and predictable tool influence function; thus it is imperative that it is fully characterized for each material that will be

http://dx.doi.org/10.5772/intechopen.75524

polished. Simultaneously, metrology is a determining factor of the final quality of the surface, since it limits the precision of the error maps that can be obtained. This requires the knowledge of a series of polishing parameters such as tool velocity, pressure and height as well as slurry type, temperature, etc. Most of these parameters remain constant during the time periods required for polishing small optics, i.e. a few minutes. If larger, meter-class surfaces need to be polished, it is important to control and keep all parameters constant during an entire polishing run, which can represent over 10 h. Thus, a very stable and precise process control of the process is required.

The HyDRa tool removal function is based mainly on four independent operating parameters: propelling air pressure, grit mass concentration, height of the tool over the surface to be polished, and slurry flow and/or slurry pressure. In order to ensure deterministically polished surfaces, the errors contributed by each of these factors must be taken into account and precisely controlled to 1% for the entire length of the polishing run (over 100 h). Simultaneously, metrology is crucial for determining the surface's final quality, since it dictates the limit of the precision of the error maps that can be obtained.

4.1. Deterministic polishing

To maximize polishing performance, an abrasive foam is created in the tool's first stage. This raises the velocity of the polishing particles, improving the removal of material. This foam is produced by combining a constant flow f (a few ml/s) slurry, with air that is kept at a constant pressure P_p. This fluid is then accelerated with pressurized air at a propelling pressure P_T, in one or more cylindrical cavities. The resulting abrasive foam is then expelled through the tool's nozzle, where a vortex is produced that develops into a radial flow, and generates a grazing, uniform removal footprint. A relation of slurry flow f to slurry pressure P_p exists for each value of accelerating pressure P_T. This, in addition, depends on the tool's physical characteristics, such as its overall dimensions, the geometry of the acceleration chamber(s), as well as the nozzle shape. This relation establishes an operational diagram that defines tool bias. In this section, the control of f is chosen, although it is possible to select to control for either f or P_p. The removal D of HyDRa mainly depends on four independent operating parameters: propelling air pressure P_T, grit mass concentration ρ_i, slurry flow f, and distance of the tool over the workpiece Z. In order for deterministically polished surfaces to be obtained, the errors contributed by each of these parameters must be taken into account and controlled.

The removal rates, as determined by a series of independent experiments, where the polishing parameters varied, are shown in **Figure 9**.

To generalize the analysis, all parameters X are normalized around their operational values as x/x^-. With this, the relative variation of each parameter, defined as $\delta X = \frac{\Delta X}{X^-} = \Delta\left(\frac{X}{X^-}\right)$, is computed. The ratio between the relative variations of removal rate and the relative variations of each polishing parameter is given in the upper-left corner of the graphs. Here the operational value for the relative density is 80 g/l. As can be seen, removal rate varies as 1.18 times the fluctuations in the concentration. The relationship between the removal rate and the rest of the parameters can be determined similarly, where the fluctuations around the operation point of each parameter are taken into account. The sensitivities on

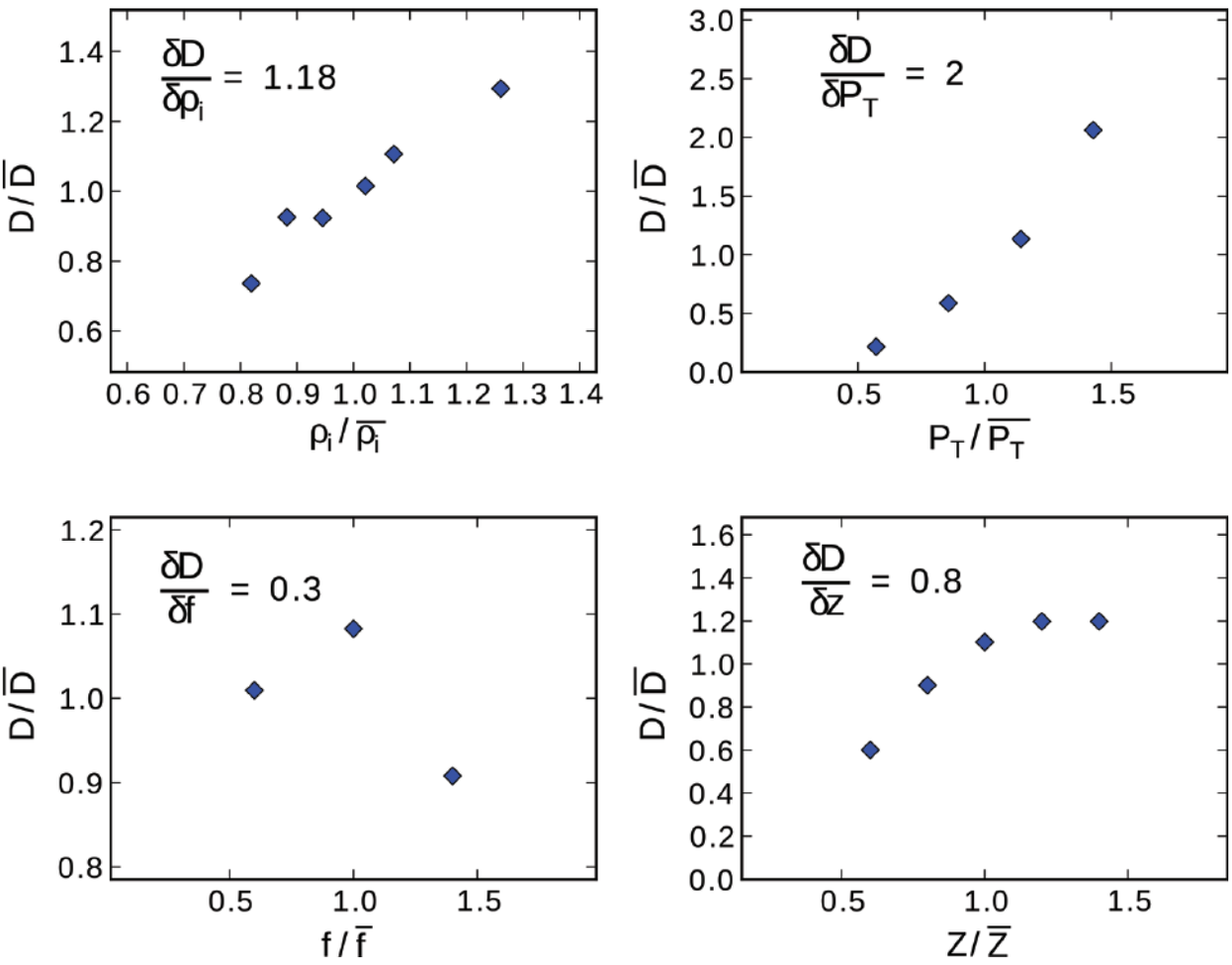

Figure 9. *N*ormalized removal rate D/D^{-} (dimensionless) with reference to the normalized value of certain polishing parameters (mass concentration ϱ_i, propelling pressure P_T, slurry flow f and tool height *z*). The sensitivity of removal to each parameter is indicated in the upper left corner of each graph.

propelling pressure P_T (upper-right), slurry flow *f* (lower-left) and tool height *z* (lower-right) are 2, 0.3 and 0.8, respectively. In this test, the operation points were 40 PSI, 5 ml/s and 400 μm, respectively. An optimum value of slurry flow (around 5 ml/s), for which the removal rate is maximized and which is chosen to operate the HyDRa tools, can be found. Removal only decreases slightly for higher or lower flow rates around this value. This is shown in the lower left panel of **Figure 9**.

In the case of tool height *z*, load cell force F_c can be used instead, since, as shown in [4] tool force is an approximate linear function of distance when close to the operation point, given that $z + K F_c$, with $K \sim 10$ μm/N, and hence $\delta z = \delta F_c$.

If we assume that each of these four variables is statistically independent, the total error can be added in quadrature. For example, if each parameter is controlled to ~1% precision, then the total error δD_T is $\delta D_T = \sqrt{(1.18 * \delta\rho)^2 + (2 * \delta P_T)^2 + (0.3 * \delta f)^2 + (0.8 * \delta z)^2}$, which amounts to 2.5% for this case. This means that if 500 nm of material are removed in one polishing run, considering that the parameters are controlled to 1%, the total surface error results in 12.5 nm RMS (λ/50). This constitutes a 2.5% level of nondeterminism (i.e., 97.5% determinism).

http://dx.doi.org/10.5772/intechopen.75524

4.2. Polishing example: polishing of an 84 cm mirror

As mentioned before, in order to deterministically polish large surfaces it is imperative that removal rate remains stable over extended time periods. We polished an 84-cm hyperbolic primary mirror to $\lambda/10$ RMS, 0.7 λ PV in order to prove that HyDRa could deterministically tackle meter-class optics. The polishing process is described in [12]. From the error maps that were acquired during the iterations, the level of determinism of the process could be calculated. From each map we computed a tool trajectory with distinct dwell times. The amount of removed material was calculated by subtracting the previous error map from the measured one. Then, from the obtained result after polishing, the removed material for each iteration was determined and plotted as a function of dwell time. Refer to **Figure 10**. A linear relation is expected and the deviation from this represents the level of determinism, **Figure 11**. This experiment was useful to evaluate the importance of the stability of each parameter in the level of determinism for prolonged time periods. In the figure, a larger error can be noticed for shorter dwell-times than for longer ones. This is due to CNC errors when the tool has to be quickly accelerated to obtain short dwell-times. As the mirror is progressively corrected, the surface is smoother and these changes tend to decrease.

4.3. Polishing example: PSD and polishing of Fabry-Perot etalons

Three components in the power spectral density (PSD) of the residual surface errors that are related to the footprint diameter of the tool D_H exist for any given polishing method. In the low frequency domain ($L >> D_H$), the surface errors (optical figure) are a function of the stability of the polishing parameters during the polishing run, while at the high-frequency domain ($L << D_H$), the physics of the polishing process determine surface quality (micro-roughness). In the case of mid-spatial frequencies ($L \sim D_H$) surface quality depends on the geometry and overlap of the polishing trajectories. We obtained PSD measurements as described in [4] and references therein.

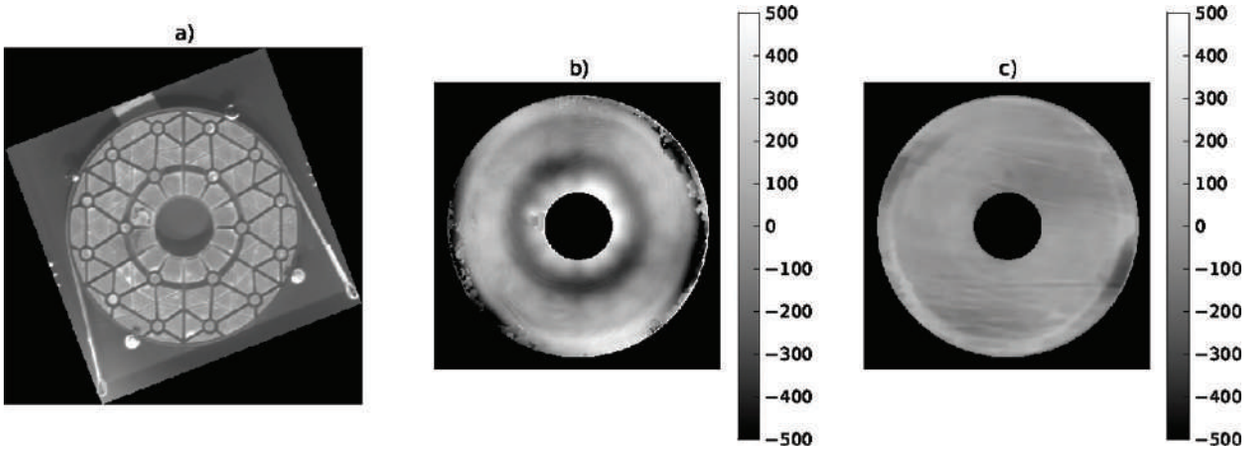

Figure 10. An 84 cm mirror with a 1 cm thick faceplate that was polished using the HyDRa system. (a) Picture of the mirror's internal back-structure. (b) Mirror prior to HyDRa finishing. The print-through left by the original lap-polishing process can be noted. (c) Mirror surface after HyDRa polishing. The polishing process entirely removed the print-through by polishing with the zero-force, error-map based process described in this chapter. Low-order Zernikes have been removed so this effect is highlighted. Z-scales are the same and are shown as vertical bars in nm.

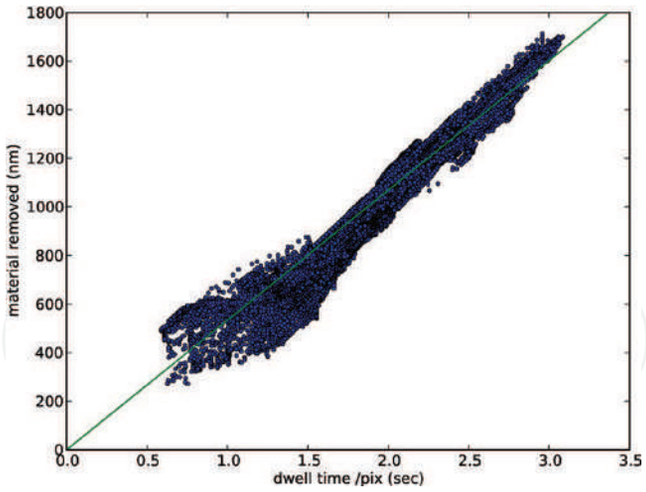

Figure 11. Total amount of material removed in the final iteration (3 runs = 30 h), as a function of dwell time in each area element of 2.6 × 2.6 mm^2 (pixel size). A linear relation at a removal rate of 13 mm^3/h (shown as a solid line) is expected for an entirely deterministic process. The true deviations from this behavior amount to 10.6%, which is the attained level of non-determinism and represents the standard deviation of the points with respect to the best-fit line.

The PSD is discussed using the results obtained while polishing four 50 mm etalon plates to better than $\lambda/100$. These 50 mm diameter water-free fused silica plates are used in an NIR scanning Fabry-Perot interferometer. These surfaces were polished using the HyDRa tool discussed in Section 4. Surface measurements were taken with a phase-shifting (PS) Fizeau interferometer in order to quantify the figure with a 180 μm pixel size projected onto the surface. A PS Linnik interferometer with 2× and 50× objectives (equivalent pixel sizes of 7.6 and 0.16 μm) was used to determine mid- and high-spatial frequencies, respectively. In **Figure 11a**, the 2-dimensional power spectrum PSD_2 vs. spatial frequency is plotted. It can be noted that three overlapping regimes exist that correspond to the series of instruments that were used to evaluate the surface quality. The integrated RMS values for each regime are 3.8, 1.5 and 2.9 nm for low-, mid- and high-spatial frequencies, respectively. The overall slope is approximately described as $f^{-2.5}$. Since in this section the physics of the HyDRa tool are described, emphasis will be made on the PSD high spatial-frequencies (micro-roughness). For lower frequencies, i.e. meter-class optics, where it is crucial to achieve a very high stability of the operational parameters, refer to [13]. **Figure 12b** shows one of four etalon plates that were polished.

Interferograms [10] showed initial figure errors that ranged between 27 and 83 nm. Using these measurements, we calculated the error maps to compute a dwell-time based raster pattern trajectory for the CNC polishing machine. An acceleration pressure of 40 PSI was chosen and tool height was controlled to achieve zero-force on the workpiece. RMS surface qualities between 3.6 and 6.8 nm were obtained after two 15 min polishing runs. The low frequency interval of the PSD shows an overall RMS fit to the desired figure of 3.8 nm, which is in accordance with the results presented in the previous section: a final surface figure quality of $>>\lambda/100$ for visible wavelengths. Sub-aperture polishing can introduce unwanted patterns associated with the polishing trajectories [14] which can occur in HyDRa polishing with a 7 mm footprint on a 40 mm sample. To minimize these mid-spatial frequencies, the tool was raster-scanned with 0.25 mm steps, which corresponds to 1/20th of the tool's footprint size.

http://dx.doi.org/10.5772/intechopen.75524

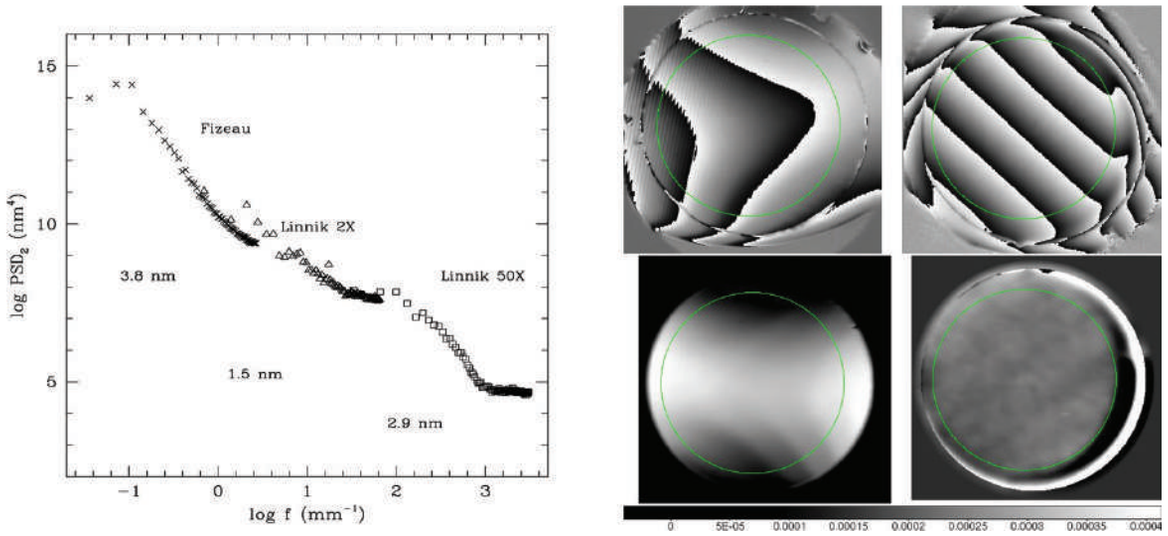

Figure 12. (a) 2-D power spectral density PSD_2 as a function of linear spatial frequency obtained with HyDRa on an etalon plate. (b) One of four etalon plates prior and after HyDRa polishing. The wrapped phase of the surface before (left) and after (right) polishing is shown in the upper images. Unwrapped phases of the original and polished surface, respectively (lower images). The inscribed green circle delimits the plate's usable region. Of the 50 mm plate diameter, only the central 40 mm were polished, since the exterior ring is used for mounting the plates. This area is indicated within the light-colored circle.

Traces of this raster pattern should have been visible in the 0.14–4 mm^{-1} frequency range on the PSD. However, no evident peaks that could have been related to grooves left by a raster pattern could be observed, and only a tiny peak corresponding to about 100 μm could be noted. This peak adds a very small fraction of a nm to the total 1.5 nm RMS of the mid-frequency band, demonstrating that "over-rastering" can be effective in minimizing mid-spatial frequencies. This represents an alternative to the approach proposed by Fähnle [15], using only one tool. A comparatively large footprint has the extra advantage of making our process insensitive to CNC positioning errors, which are two orders of magnitude smaller than the footprint size. Finally, the high-spatial frequency domain shows an RMS of close to 3 nm. Although the PSD decreases in this region, it apparently stabilizes at frequencies $>10^3$ mm^{-1} or sizes smaller than 1 μm. This number is related to the grit size that was used in this test. To sustain a decreasing PSD tendency and thus, smaller values of the high-frequency RMS, the use of smaller grit sizes is suggested. Integrating the high-frequency domain of the PSD to obtain the RMS is also equivalent to calculating the RMS directly from a 50 × 50 μm area of the micro-interferogram, according to a standard definition of micro-roughness [16]. This micro-roughness obtained with the HyDRa process (3 nm) is comparable to the roughness reported in current FJP literature [5].

Acknowledgements

This work was funded by Universidad Nacional Autónoma de México DGAPA-PAPIIT grants IN112505, IN115509, IT100216 and IT100118, as well as by Instituto de Astronomía, UNAM.

Author details

Erika Sohn*, Esteban Luna, Elfego Ruiz, Luis Salas and Joel Herrera

*Address all correspondence to: sohn@astro.unam.mx

National Autonomous University of Mexico (Universidad Nacional Autónoma de México), Institute for Astronomy, Ensenada, BC, México

References

[1] Ruiz E, Sohn E, Salas L, Luna E. Hydrodynamic radial flux tool for polishing and grinding optical and semiconductor surfaces. 2007. US Patent 7169012

[2] Ruiz E, Sohn E, Salas L, Luna E. Modulo mezclador para una herramienta hidrodinamica deterministica para el pulido pulsado de superficies opticas, y metodo para llevar a cabo el pulido pulsado. PCT Patent Application. UNAM.REG.OMPIPCT/MX/a/2016/016317

[3] Li Z, Li S, Dai Y, Peng X. Optimization and application of influence function in abrasive jet polishing. Applied Optics. 2010;**49**:2947-2953

[4] Sohn E, Ruiz E, Salas L, Luna E, Herrera J. HyDRa: Polishing with a vortex. Applied Optics. 2013;**52**:6146-6152

[5] Fähnle OW, van Brug H, Frankena H. Fluid jet polishing of optical surfaces. Applied Optics. 1998;**37**:6771-6773

[6] Shi C, Yuan J, Wu F, Wan Y. Ultra-precision figuring using submerged jet polishing. 2011. COL 092201

[7] Arnold T, Böhm G, Fechner R, Meister J, Nickel A, Frost F, Hänsel T, Schindler A. Ultra-precision surface finishing by ion beam and plasma jet techniques-status and outlook. Nuclear Instruments and Methods in Physics Research A. 2010;**616**:147-156

[8] Guo P, Fang H, Yu J. Edge effect in fluid jet polishing. Applied Optics. 2006;**45**:6729-6735

[9] Joel HV, Esteban Antolin LA, Fernando QP, Elfego Guillermo RS, Luis SC, Erika SL. Programa de Computo de Evaluacion de Error Ygeneracionde Trayectorias HYTPT. Software Copyright, Universidad Nacional Autonoma de Mexico, 03-2012-120612154800-01. Mexico: INDAUTOR; 2012

[10] Luna E, Salas L, Sohn E, Ruiz E, Nunez JM, Herrera J. Deterministic convergence in iterative phase shifting. Applied Optics. 2009;**48**:1494-1501

[11] Salas L, Luna E, Sohn E, Ruiz E, Herrera J. HyDRa: Polishing process convergence rate optimization. Applied Optics. 2013;**52**:7007-7010

[12] Sohn E, Ruiz E, Salas L, Luna E, Herrera J, Quiros F, Nunez M, Lopez E. Polishing results of an 84 cm primary mirror with HyDRa. In: Proceedings of the SPIE Optifab, TD07-17; 2011

[13] Ruiz E, Salas L, Sohn E, Luna E, Herrera J, Quiros F. HyDRa: Control of parameters for deterministic polishing. Optics Express. 2013;**21**:20334-20345

[14] Dunn CR, Walker DD. Pseudo-random tool paths for CNC sub-aperture polishing and other applications. Optics Express. 2008;**16**:18942-18949

[15] Fähnle O, Mourad S, Hauser K, Meeder M. Detection and removal of spatial mid-frequencies in sub-aperture finishing. In: OSA IODC OFT, OWE4; 2010

[16] Nunez M, Salinas J, Luna E, Salas L, Ruiz E, Sohn E, Nava A, Cruz-Gonzalez I, Martinez B. Surface roughness results using a hydrodynamic polishing tool (HyDra). SPIE. 2004;**5494**: 459-467

IntechOpen

Chapter 6

Additives for Abrasive Materials

Artur Jamrozik, Łukasz Klapiszewski,
Beata Strzemiecka, Adam Voelkel and
Teofil Jesionowski

Additional information is available at the end of the chapter

http://dx.doi.org/10.5772/intechopen.74822

Abstract

The overarching objective of the chapter is to acquaint the readers with the topic associated with the production of abrasive tools and presentation of the most significant research results regarding the determination of the most important functional properties of selected additives (described in the literature and established on the basis of authors' own scientific experiences). The studies regarding various additives, which were characterized in detail in the literature, were mainly based on thorough physicochemical and microstructural analysis as well as the determination of basic strength and thermos-mechanic parameters. The attempt to implement alternative cross-linking agents, which would result in the limited release of volatile organic compounds, is also of great importance in terms of production of environmentally friendly final products. A subsequent aim is to attract the attention of a wide range of readers and popularize the topic associated with conventional abrasive materials and next-generation abrasive compositions.

Keywords: abrasive machining, abrasive tools, binders, functional fillers, biopolymers

1. Introduction

Modern abrasive tools used in industry are required to fulfill a number of conditions relating to quality, durability and performance. Progress in a wide range of areas related to materials engineering has made it possible to use abrasive machining in place of complex specialized processes. Recent work on the development of abrasive tools has been focused on the search for functional additives, above all to improve the functional properties of the product through the addition of fillers that primarily increase adhesion between the grains and binder. Another key issue is to obtain more environmentally friendly final products by reducing the quantities

of harmful compounds released, which can be done by using alternative cross-linking agents. In this chapter, the authors focus above all on the aforementioned questions, describing both the current state of knowledge and likely directions of future development in these areas.

2. The basics of abrasive machining

Abrasive machining is the most popular method of finishing, in which an abrasive tool (usually in the form of a grinding wheel or disk) rotating at high speed is used to remove the surface layer of a softer material. In modern industry, grinding technology is constantly being developed, in line with specific requirements applicable to a wide range of products and processes. Grinding is a key stage in the technology of production for advanced products and surface treatment in many fields of industry. The technique has many advantages over other surfacing methods.

A grinding process can be used for precise operations in the production of high-quality parts, with high accuracy and small dimensional tolerance [1]. It can be used to produce both very large machine parts and small objects such as optical instruments, elements of electronic devices, silicon wafers and rolling bearings. Another invaluable feature is the possibility of adjusting the abrasive machining process to remove large quantities of material in a short time. High grinding performance is necessary when it is required to remove a significant quantity of the machined material in a single fast operation. This applies, for example, in the cleaning of castings in foundries. Abrasive machining is also a technique used in working with very hard materials and hardened surfaces. In many cases, it is the only feasible method of finishing the surface of hard materials. The increasingly popular use of inorganic materials composed of ceramics and hard minerals with a crystalline structure enables the elimination of problems related to the finishing of surface layers. Such operations are applied, for instance, in the aerospace industry.

Figure 1 shows the grinding process in diagram form. Six basic elements may be identified: the grinding wheel, the worked material, the coolant or cutting fluid, the machine tool, the surroundings (air) and material chips.

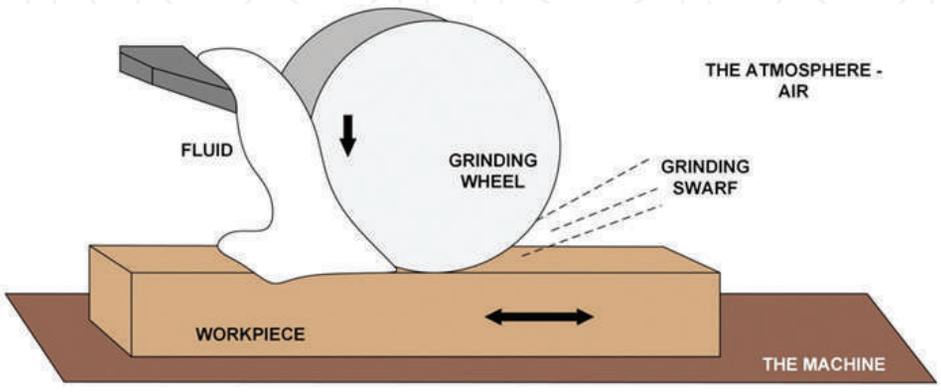

Figure 1. Simplified diagram of the grinding process, adapted from [2].

The most important elements playing a role in the process are the abrasive tool and the processed material. It is their properties that have a decisive impact on the course and effect of abrasive machining. Parameters of the grinding wheel, such the grain size and type, hardness, rigidity, and physical and chemical properties, determine its suitability for the machining of a given material. The choice of an appropriate tool is also dependent on the shape, hardness and physicochemical properties of the worked surface, and it is therefore essential to perform a full analysis of the material being processed [2, 3]. The process is also influenced by chemical factors. Atmospheric oxygen and high temperature favor the formation of oxides on the metal surface, which improves lubrication. Often, however, a coolant or cutting fluid is additionally used; this draws excess heat from the worked material and the tool, as well as reducing friction and extending the lifetime of the grinding wheel. Because of the greater stability of a cooled process, its accuracy can be improved and heat damage can be prevented. The technical condition of the machine tool is also important. Its purpose is to provide static and dynamic restriction of displacements between the tool and the worked object. The high quality and stability of the machine tool are therefore of key importance for achieving the desired tolerance in terms of geometry, dimensions and roughness. Unwanted vibrations of the machine may cause cracking and accelerated wear of the abrasive grains [4].

3. Abrasive tools

An abrasive tool is a composite material in which the continuous phase (matrix) consists of a binder, while the dispersed phase is an abrasive grain. Apart from these two basic components, additives are used in the form of fillers—active and inactive—which serve either to improve the technical parameters (active fillers) or to reduce the production cost of the tool (inactive fillers). A diagram of the structure of an abrasive tool is shown in **Figure 2**.

The industrial process of production of abrasive tools with an organic binder comprises three principal stages: mixing of components, molding, and firing (annealing) to provide cross-linking of the binder [5, 6].

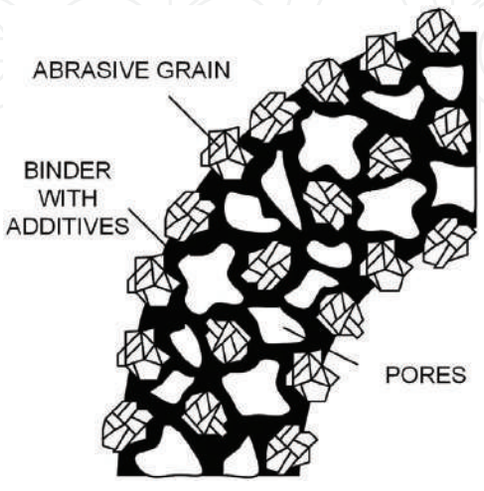

Figure 2. Simplified diagram of the structure of an abrasive tool, adapted from [2].

The mixing of the components of the tool begins with covering of the surface of the grains with liquid resin or a solvent (such as furfuryl alcohol). The uniformly moistened grains are then mixed with powdered resin, with the addition of fillers. The resulting mixture is sieved to remove lumps or agglomerates. The mixing of the components is a very important process: too loose a consistency may cause inhomogeneity of the final product, while excessive wetness will lead to difficulties in further processing.

The next important stage of the preparation of abrasive materials is molding, which may be hot or cold. Cold molding is applied in the case of tools in which pores account for at least 10% of the volume, and the pressing time does not usually exceed 1 min. Hot molding is used in the production of non-porous grinding wheels of high density. In this case, the pressing time is longer, between 20 and 60 min, and the temperature may be as high as 150°C.

The final process is the firing of the molded prefabricated elements. This is done in industrial furnaces, according to a strictly defined temperature program. The length of the program depends on the size of the tool—with larger tools, the increase in temperature should be slower and the duration of the program as a whole should be longer. In most cases, the cross-linking process lasts between 18 and 35 h, and the temperature does not exceed 200°C (or usually 180°C).

4. Abrasive materials

Abrasives are natural or synthetic materials which are used in a highly fragmented state (usually in the form of grains) as a basic component for the production of abrasive tools. Synthetic abrasive materials may be obtained by:

- electrothermal melting processes (synthetic corundums);
- in-furnace processes between solid and gas phases (silicon carbide);
- high-pressure processes (superhard materials such as synthetic diamond and cubic boron nitride);
- sintering processes (sintered corundums).

For a material to serve as an abrasive, at least one basic condition must be fulfilled. If a layer of material is to be removed by abrasion, the ratio of the hardness of the abrasive H_s to the hardness of the worked material H_m must exceed a certain minimum value. In the great majority of cases the H_s/H_m ratio is in the range 1.5–2.0. The hardness parameter is therefore the principal criterion determining whether or not a material can be classed as an abrasive. Another very important parameter is the material's melting point. Even in the early 1960s it was shown that during the grinding of metals the temperature may rise high enough to cause the metals to melt. This implies that abrasive materials should not have melting points below 1600°C. Due to this criterion, all known organic substances and almost 99% of inorganic substances are excluded from use as abrasive grains. A further surprising fact is that there is no known hard material containing more than four atoms. The most commonly used abrasives

are boron carbide, silicon carbide, synthetic corundums (standard, noble and modified), diamond (mainly synthetic) and cubic boron nitride. A classification scheme for natural and synthetic abrasive materials is shown in **Figure 3**.

4.1. Silicon carbide

Silicon carbide, also known as carborundum, is a compound of carbon and silicon with the condensed formula SiC, composed of 70.045% silicon and 29.955% carbon. It was the first abrasive material to be obtained by synthesis. The compound was discovered by the Cowles brothers in 1885, when they were attempting to melt quartz in an electric arc between carbon electrodes. It was first produced industrially in 1891 in the United States, by the Carborundum Company founded by Edward G. Acheson, who was officially recognized as the originator of the method of production of SiC. Silicon carbide may crystallize either in a hexagonal arrangement (α-SiC) or in a cubic arrangement (β-SiC) [7]. The atoms in the SiC crystal lattice form two interpenetrating tetrahedral structures. SiC is resistant to the action of molten metals such as Al, Cu, Pb, Sn, Zn, Cd, although it is sensitive to Fe, Ni, Cr, Co, Mn, since these metals are capable of forming alloys with SiC. It is not damaged by acidic slags or salts, although damage

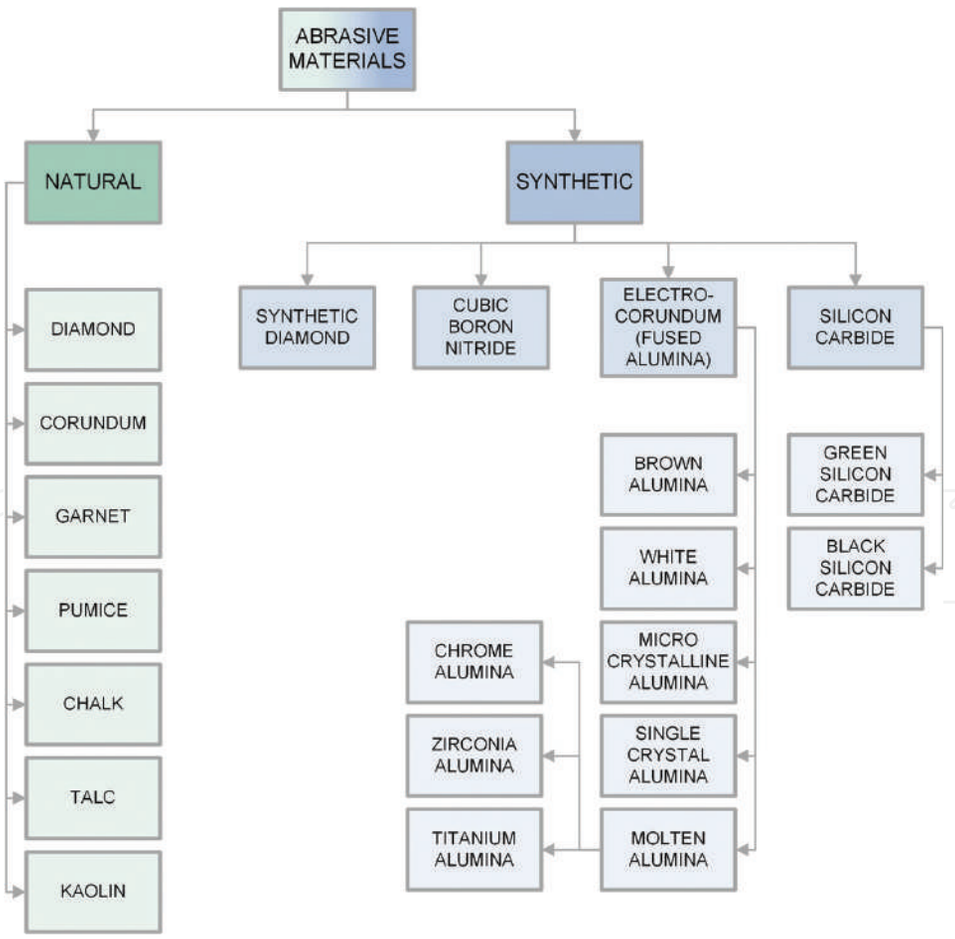

Figure 3. Classification scheme for natural and synthetic abrasive materials, based on [4].

is caused by molten alkaline compounds, including certain hydroxides and salts. Sample reactions with such compounds are given below in Eqs. (1) and (2):

$$SiC + Na_2CO_3 + 2O_2 \rightarrow Na_2SiO_3 + 2CO_2 \quad (1)$$

$$SiC + 2KOH + 2O_2 \rightarrow K_2SiO_3 + H_2O + CO_2 \quad (2)$$

At high temperatures, SiC is able to react with certain oxides (above 800°C), including CuO and PbO, and with oxides of magnesium and calcium (above 1000°C). Up to 900°C, its stability is not significantly affected by oxygen, but above that temperature, the surface is fairly strongly oxidized. The products of this reaction may be compounds such as CO, CO_2, SiO and SiO_2. The role of oxidizing agent may also be played by steam or carbon(II) oxide [8].

Silicon carbide has found many applications in various branches of industry. Because of its high mechanical strength, hardness, and ability to form relatively thick crystals, it is used chiefly as an abrasive material in abrasive tools. Somewhat less frequently, it is also used to produce fire-resistant materials such as retorts, crucibles, furnace linings, bricks, and pipes in heating systems. This is possible because of its very high thermal conductivity, resistance to sudden temperature changes, and high decomposition temperature. Silicon carbide also offers high electrical conductivity, and can thus be used in electrical engineering to produce heating elements, resistors, diodes and transistors [8, 9].

4.2. Synthetic corundum

Synthetic corundum is a material whose principal component is crystalline α-Al_2O_3 (corundum). It also contains other compounds, chiefly oxides of silicon, titanium, iron, calcium and magnesium. It can be produced in a Higgins electric arc furnace. The main raw material used to obtain ordinary synthetic corundum is bauxite. Synthetic corundum is highly resistant to the action of practically all acids and bases, both organic and inorganic. Only at high temperatures (above 900°C) does it react with molten salts of alkaline metals, producing aluminosilicates. Hydrogen causes the reduction of corundum to suboxides of aluminum, although this occurs only above 1400°C. Carbon in large excess is able to reduce Al_2O_3 at temperatures above 2000°C [10].

Synthetic corundum is used practically exclusively for the manufacture of abrasive tools. Its abrasive ability is largely dependent on the quantity of additives. Apart from standard synthetic corundum, which is produced in the largest quantities, there are also other varieties, such as [11]:

- White alumina—this material contains significantly fewer impurities than standard synthetic corundum. It is generally laid down that noble synthetic corundum should not contain less than 98.5% aluminum oxide. The principal feature of this material is the possibility of self-sharpening of the abrasive grains during operation of the tool. Synthetic corundum grains have slightly lower mechanical strength, and so when the cutting edge of the crystal becomes blunted it is chipped off the tool, thus uncovering fresh, unblunted layers. This property is particularly desirable when very accurate working is required and when the tool is to apply a low pressure on the worked material.

- Modified synthetic corundums—these are materials based on aluminum oxide, produced with the addition of compounds that are able to become incorporated into the corundum crystal lattice and form solid solutions with it. The parameters of the final product can be controlled by varying the quantity and type of modifier used. The most commonly encountered modifiers are:
  - chromium oxide (Cr_2O_3)—this modifier is used to produce pink alumina, a material that has a greater quantity of crystals than white alumina, better abrasive ability, unchanged microhardness, but slightly lower mechanical strength;
  - titania (Ti_2O_3)—this modifier produces a material with high abrasive ability and greater microhardness than white alumina;
  - zirconia (ZrO_2)—this produces a material with high ductility and mechanical strength.
- Monocorundum—this is a variety of synthetic corundum with greater grain isometry and smoother faces. It has higher microhardness and mechanical strength than other varieties of synthetic corundum. Like white alumina, it has self-sharpening capacity. Because of the lower power of grinding when monocorundum is used, the worked surface heats up to a lesser degree, and this helps to prevent defects such as cracks and burn.

4.3. Synthetic diamond

Diamond is one of the allotropic varieties of carbon, and is unquestionably the hardest mineral occurring on Earth (with a hardness of 10 on the Mohs scale). Since the quantity of mined diamond is insufficient to meet supply, leading to very high prices, it has proved necessary to develop a method for synthesizing diamond. This was achieved for the first time by the Swedish company ASEA in 1953. Since that time, annual production of artificial diamonds has been continuously increasing.

Diamond has a density of 3.5 g/cm^3. Its crystal lattice has the form of a cube containing 18 carbon atoms [12]. All of the carbon atoms in diamond are joined by high-energy covalent bonds, which give the material its exceptional hardness. Another important property is its very good thermal conductivity, which enables heat to be removed efficiently during grinding. It also has a small thermal expansion coefficient, which reduces thermal deformation of tools with diamond grains. Another very important feature is anisotropy of hardness and grindability. These parameters vary not only between different planes, but also depending on the direction in which the force acts in a given plane. The material is resistant to the action of very strong acids and their mixtures, but dissolves in molten hydroxides and salts such as $NaNO_3$ and KNO_3. It also dissolves in molten iron and its alloys above a temperature of approximately 800°C. In the presence of air it combusts at a temperature from 850 to 1000°C. Synthetic diamonds also have several features that distinguish them from natural diamonds. They are usually smaller (with an average size between 0.2 and 0.4 mm) and have different grain shapes and a rougher surface. Surface roughness, and crystal vertices with smaller angles and smaller radii of curvature are desirable features for abrasive machining. Since the content of impurities in synthetic diamonds is higher than in natural diamonds, parameters such as

mechanical strength and brittleness are somewhat inferior. Processes for synthesizing diamond are carried out at high pressures (reaching 10 GPa) and high temperatures (up to 3000°C) [13, 14].

Because of its properties, diamond is used successfully for the machining of cemented carbides and ceramic sinters, for cutting glass panels, for the working of optical glass, and for making measurements of hardness and smoothness of surfaces.

4.4. Boron nitride

Cubic boron nitride (borazon) is, like diamond, a member of the group of superhard abrasive materials. Due to the similarity of the hexagonal form of boron nitride (α-BN) to the structure of graphite, it was predicted by analogy that the compound must also exist in a diamond-like form (β-BN). This was proved in 1957 by Robert H. Wentorf, who became the first to successfully synthesize cubic boron nitride [15]. Its crystal lattice has a similar structure to diamond. Of the 18 atoms contained in a cube, four are boron atoms and the remainder nitrogen. Unlike diamond, in which all bonds are covalent, in cubic boron nitride 75% are covalent bonds and 25% ionic. This fact is significant for the mechanical properties of Borazon: its hardness and mechanical strength are lower than those of diamond. The material is exceptionally thermally stable in atmospheric air (up to 2000°C at normal pressure), being transformed back to the hexagonal form only above 2500°C. However, it is sensitive to the action of water, which at high temperature causes its decomposition into boric acid (H_3BO_3) and ammonia. This needs to be taken into account when selecting a filler whose decomposition products include H_2O. Synthesis of β-BN is carried out in the presence of catalysts (such as metallic potassium) at pressures of 6.5–9.0 GPa and temperatures of 1500–2000°C [16, 17].

Borazon is not used for the machining of such hard and brittle materials as glass, ceramics and granite, for which the use of tools based on synthetic diamonds is recommended. Nevertheless, it offers excellent performance in the working of tool steels, as well as other metals and alloys. Tools containing β-BN can produce a ground surface of high quality, thanks to low grinding power and lower temperatures of abrasive machining.

4.5. Modification of abrasive grains

Conventional abrasive materials that perform well in typical abrasive machining may prove insufficiently effective in a chemically aggressive environment or when high temperatures and grinding pressures are used. To improve the functional properties of the abrasive grain and the tools based on it, one of two routes may be selected—modification of conventional abrasives to improve their functional parameters, or the development of new methods of producing superhard materials (or improvement of existing methods) with the aim of reducing costs. Conventional abrasive materials are usually subjected to thermal or thermal-chemical processing, although more and more research is being done into the surface modification of abrasive grains.

Thermal processing is among the oldest and most popular methods of modifying raw abrasive grains. It enables reduction of the brittleness of grains, particularly those of synthetic corundum, by means of roasting at temperatures up to 2000°C. This results in the creation on the grain

surface of a fine crystalline structure, which increases its operational durability and the stability of its machining properties. Roasting is carried out to eliminate undesirable impurities: sodium and potassium 11-aluminates, described as β-Al_2O_3. The presence of aluminates in the grain may also reduce the mechanical strength of a single grain by as much as 30%. As a result of thermal processing, β-Al_2O_3 corundums in the form $K_2O{\cdot}11Al_2O_3$ transform completely into α-Al_2O_3 at a temperature of around 1520°C, while $Na_2O{\cdot}11Al_2O_3$ transforms at 1700°C. The roasting temperature may be reduced to 1300°C if gaseous hydrogen is used [18].

Abrasive grains are also modified to reduce the adverse impact of water-based coolants, which usually shorten the tool's lifetime. The reason for the reduced durability is the tendency of resins to crack under the influence of water, causing the grains to become loose and fall out. A way of preventing this may be to cover the grains with a layer of modifier containing hydrophilic and/or hydrophobic components. Hydrophilic components used include silanes containing amine, ureide, isocyanide, acetoxy and chloride groups. Hydrophobic silanes contain mainly phenyl, vinyl, methacrylic or epoxide groups. Surface modification using a dual-component silane-based modifier brings several undoubted benefits. The hydrophilic component covers the entire surface well, at the same time facilitating its moistening. The hydrophobic component may be applied together with the first component or as a separate layer, demonstrating the ability to bond with both the covered grains and the resin binder. Such modification prevents water-based coolants from penetrating to the interior of the tool, and thereby extends the tool lifetime, improves the material removal rate (MRR) and enhances the overall quality of the finished surface [19].

The development of innovative abrasives involves not only the modification of conventional materials but also the creation of new methods for producing superhard materials (superabrasives). The production of such materials, primarily synthetic diamond and cubic boron nitride, originally required high temperatures and very high pressures. To convert graphite to diamond, a pressure of around 13 GPa and a temperature of 3000°C are required. In view of the difficulty of providing such extreme conditions, other methods are used, such as solvent catalyst synthesis. This method makes it possible to reduce the high activation energy and the required pressure and temperature by a half [20]. The catalysts used in the process dissolve graphite, enabling the carbon atoms to move and to adopt the positions appropriate to diamond. Commonly used metal catalysts include nickel, iron and cobalt, as well as rhodium, palladium, platinum and others [21]. Diamond may also be obtained using non-metal catalysts, such as hydroxides and carbonate salts [22].

Of increasing importance, however, are metastable processes of diamond synthesis. An undoubted advantage of these is the relatively simple equipment required to produce diamond film and the high purity and homogeneity of the product [23]. In such processes, carbon in the form of diamond is precipitated from a mixture of hydrocarbon and hydrogen [24]. Several techniques of chemical vapor deposition (CVD) are currently applied, using microwave plasma [25], plasma jet [26], arc discharge [27] and laminar and turbulent oxy-acetylene combustion [28, 29] (see **Figure 4**). These methods require the use of high pressures and gases of relatively high purity. The gas mixture may consist of hydrogen, argon, oxygen and methane—the composition depends on the desired size of the diamond grains [30–32]. Methods have also been developed which reduce the use of harmful and expensive gases, including a

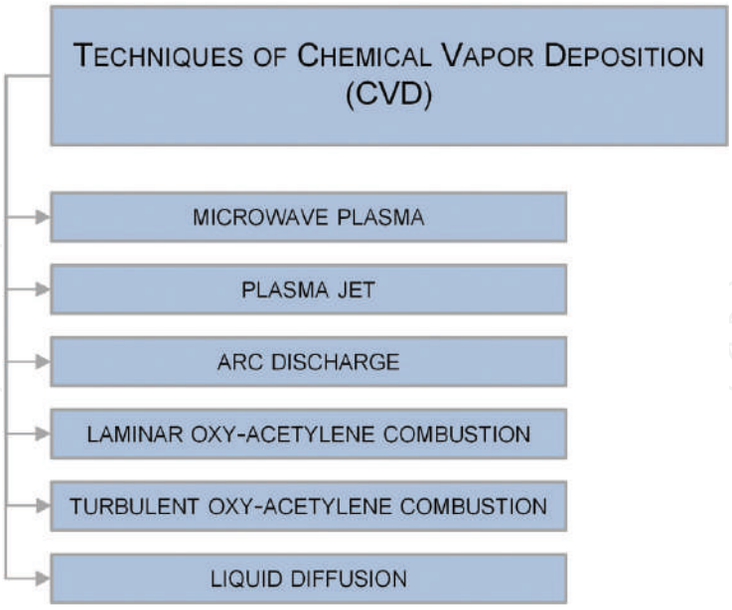

Figure 4. Techniques of chemical vapor deposition (CVD).

liquid diffusion method with methanol as a source of carbon, carried out in an argon atmosphere under microwave energy. This method can produce a film with a diamond content of approximately 75%, while reducing the risk associated with the use of explosive gases such as hydrogen and methane [33].

Another interesting study concerns the obtaining of single-phase nano-polycrystalline diamonds using direct conversion from graphite under high temperature and ultra-high pressure. This product offers very high mechanical strength, and does not exhibit anisotropy of its mechanical properties. Moreover, such a material does not require any additional binders, and this fact also has a positive effect on its thermal stability [34].

5. Binders

In terms of quantity, the binder is the second most significant component of an abrasive tool. It serves as a continuous phase that binds the single grains into a compact, strong composite. Abrasive composites may be based on organic binders (such as rubber, organic resins and polyurethanes) or inorganic binders (ceramics, magnesite, sintered and galvanic metals). Inorganic bonds with glass-like or vitreous structures are mostly used in grinding wheels with fine grain sizes for precision operations, while resin-bonded tools are applied in heavy metal removal processes. Ceramic and resin binders are the most commonly used types. Ceramic binders are thermally and chemically resistant and also ensure the repeatability of grinding processes. Disadvantages include their brittleness and the need to apply very high temperatures when making tools from them. Technologies for producing ceramic abrasive tools are being constantly improved. A recently introduced technology is used to obtain tools bonded with Vitrium 3 [35], which enables a smaller quantity of binder to be used, increasing the tool's

performance and also making it more porous, which enables better cooling and thus less likelihood of burning of the machined surface. Ceramic binders are used to bond superhard abrasives such as diamond and cBN. For corundum abrasives, the less expensive resin binders are more often used. These are produced with the consumption of much less energy than in the case of ceramic binders: the semi-finished product is heated at 200°C, compared with 1200°C for ceramic binders. Resin binders also offer high strength and elasticity, and give the abrasive tool good properties for polishing the ground surface. Grinding wheels with resin binders are used primarily for the cutting of materials and for rough grinding operations at high machining speeds (45–100 m/s).

A disadvantage of binders of this type is their sensitivity to the action of coolants containing bases, and to high temperature. Resin binders are most commonly based on phenol formaldehyde resins.

Phenolic resins, also called phenoplasts, have a range of properties that enable them to be used in a fairly wide range of applications. They are formed by a polycondensation reaction of phenols with formaldehyde. There are two distinct types of phenol formaldehyde resins: novolacs and resoles. The processes by which they are obtained are depicted in **Figure 5**. They differ in terms of the molar ratios of reactants and the environment in which the reaction takes place. Hardening is also carried out by a different method in each case: resole is heat-hardened, whereas novolac is a thermoplastic and must be hardened using a cross-linking agent—most commonly hexamethylenetetramine (urotropine), with the further addition of HCHO (usually in the form of paraformaldehyde).

Due to the harmful properties of formaldehyde and of the ammonia emitted when novolac is cross-linked using urotropine, new hardening agents are being sought (although up to date urotropine is still the cross-linking agent most commonly used in industry). By means of modification of novolac, for example by the introduction of epoxide and amine groups [36], it is possible to obtain resins with lower levels of emission of low-molecular-weight compounds and resulting binders with greater strength and chemical and thermal resistance.

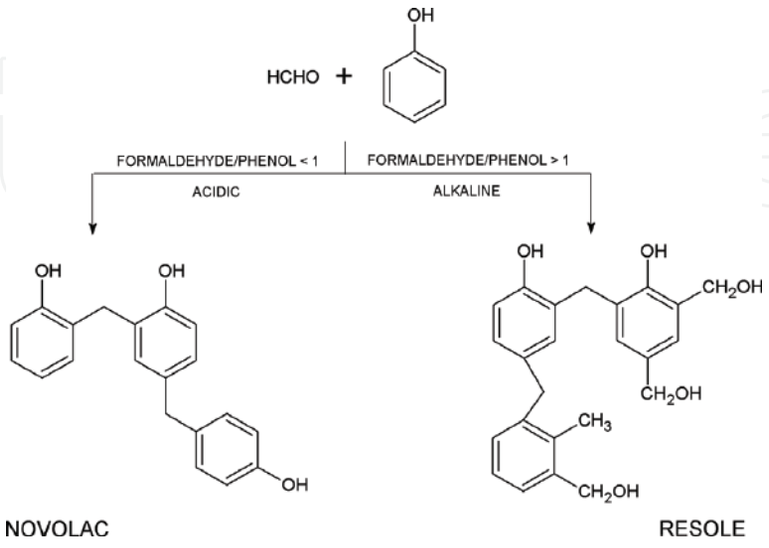

Figure 5. Reactions leading to phenol formaldehyde resins in novolac and resole form, adapted from [5].

There has been increasing interest in recent years in the use of natural raw materials to produce phenolic resins [37, 38]. However, there is still only a limited number of reports on industrial applications of abrasives containing phenolic resins based on natural materials such as lignin, which currently represents a new trend in the abrasive tools industry [39]. There would therefore appear to be a need for continued intensive research to achieve further improvements in this area, related to elimination of the existing defects of binders based on resins with the partial use of phenols of natural origin. These defects include the low reactivity of derivatives of phenol from natural sources, processing problems with abrasive articles made using them, and the inferior mechanical properties compared with tools based on traditional phenolic resins. Lignin-based resins have already been successfully used in certain demanding applications, including brake blocks [40].

A very interesting alternative to binders based on phenolic resins are benzoxazine resins. These products have a wide range of mechanical and physical properties that can be tailored to various needs. Their main advantage is the absence of emissions of low-molecular-weight compounds during their cross-linking. There is also no need to add cross-linking agents. It is also noteworthy that they are produced using phenol and its derivatives, which provides the possibility of alternative use of products of natural origin. However, it was only in 2016 that benzoxazine resins were first synthesized from lignin [41]. This area of research thus remains ripe for development.

6. Fillers

Fillers are used as an auxiliary materials in the production of abrasive tools. They are usually inorganic compounds that demonstrate affinity toward both the abrasive grains and the binder holding the grains together in the substance of the tool [42]. There are several kinds of fillers, and they can be classified according to the mechanism of their action (see **Table 1**) [43].

Possible mechanism	A description of the action
I	The first mechanism involves thermal decomposition of the filler, which leads to the emission of low-molecular-weight products (such as H_2O, HF or HCl). These reactions are endothermic, which means that the tool can operate at a lower temperature
II	In the second mechanism, the action of the filler results from its reaction with the worked surface, which causes corrosion of freshly removed fragments of metal. This prevents the chips from reacting with the abrasive and fusing back onto the worked object
III	The third mechanism is explained by the melting of the auxiliary material due to the heat produced by grinding, which leads to reduced friction (self-lubrication of the tool) and thus allows the tool to operate at a lower temperature
IV	In the final mechanism, fillers react with the machined surface. The reaction causes cracks to appear on the metal surface, making machining easier

Table 1. Examples of the mechanisms of action of different kinds of fillers.

Fillers used in a tool perform several extremely important functions:

- they increase the tool's mechanical strength by improving the adhesion of grains to the binder;
- they protect the abrasive grains from the harmful atmosphere existing in the furnace during firing;
- they prevent thermal degradation of the resin on the contact surface between grain and binder;
- they cool the tool while it is operating.

Fillers are added to abrasive composites for several reasons. Most commonly, they serve merely to reduce the production cost of the tool, through the addition of an inactive filler, usually soot, cooper slag or iron oxide. It is preferable, however, to use active fillers, which serve above all to draw heat from the process, as a result of which they undergo thermal decomposition and prevent melting of the resin binder [44, 45]. Conventional active fillers have certain drawbacks, the chief of which is the emission of harmful gases due to their decomposition. Popular fillers such as pyrite (FeS_2) and lithopone ($ZnS + BaSO_4$) emit sulfur when they decompose, while potassium fluoroborate (KBF_4), cryolite (Na_3AlF_6) and potassium hexafluoroaluminate (K_3AlF_6) emit fluorine and its compounds. Hence, at the present time, fillers are being sought that will combine desirable properties with limited adverse impact on the environment. The division into active and inactive fillers is shown in **Figure 6**.

It is worth mentioning that aluminosilicates such as natural zeolite have been successfully used as functional and ecological fillers [46, 47]. This is a cheap and environmentally friendly raw material, which also has a favorable effect on the thermomechanical properties of prototypical

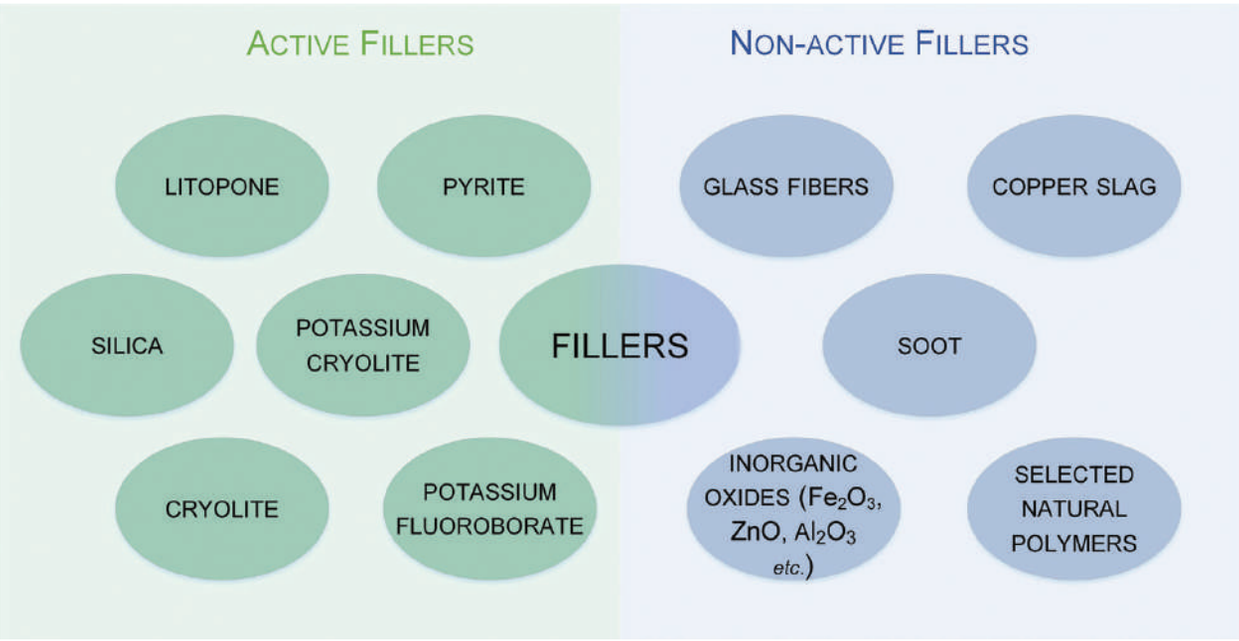

Figure 6. The division into active and inactive fillers.

resin composites used in the production of bonded abrasive tools [48]. Moreover, zeolites may accelerate the cross-linking of phenol resins [48]. Since they retain a large quantity of water in their structure [49], they should not be used for superhard abrasive tools based on cBN; since at the high working temperature of such a tool and in the presence of water emitted by the zeolites, decomposition of cBN may occur.

An interesting raw material that may be used as a filler is lignin, which offers many advantages—it is of natural origin, it is renewable, and it is produced in large quantities as a by-product of the process of delignification of wood [50]. Unfortunately, due to its characteristic structure, lignin in raw state is not able to provide the required properties [51]. Its properties can be improved in two ways. One is the activation of raw lignin via its oxidation, which enables the formation of new, more active functional groups capable of reacting with the resin binder [52]. Another way to improve the thermal stability of lignin preparations is to combine them with appropriate inorganic oxides, so as to form an organic-inorganic hybrid material [53]. Addition of these innovative materials makes it possible, above all, to improve the mechanical strength and thermal stability of the final abrasive composite.

The search for new, functional fillers, which increasingly often are hybrid materials, is intensifying at the present time. The primary goal is to produce systems with improved properties, having a decisive impact on the abrasive tool that is the final product. The combination of organic polymers or biopolymers with inorganic oxides makes it possible to obtain modern additives with previously unencountered properties. Another important factor is the cost associated with the production of abrasive materials. These can be kept relatively low by using waste products for this purpose, including wastes of natural origin.

7. Conclusions

Abrasive technology has been developed for centuries, but there still exists a wide range of opportunities for its continued improvement. In view of the development of manufacturing industry and the dynamic state of the global economy, modern abrasive tools are becoming subject to ever more rigorous requirements as regards quality, performance, durability, cost, and impact on the environment. Future development will involve further work on each of the main components of abrasive composites, as all of these have a significant effect on the functional properties of the final product. Present trends indicate that the search will continue for new, cost-effective ways of obtaining polycrystalline abrasive materials on the nanoscale, with previously unobtainable strength properties. Attempts will also no doubt be made to modify the surface of grains with organic compounds to produce on the surface functional groups capable of reacting with the groups present in resin binders. The development of binders, in turn, will be focused on reducing their toxicity by limiting the quantities of compounds emitted during the manufacture and operation of tools, while at the same time improving their mechanical properties. An excellent alternative to traditional resin binders would appear to be benzoxazine resins, which offer very interesting physicochemical parameters, low toxicity and wide possibilities of molecular design. It is equally important to seek new functional fillers for abrasive tools, especially organic-inorganic hybrid materials. This

vision is particularly attractive in view of the possibility of producing and using many different systems combining inorganic oxides with natural polymers, which in many respects appears to be an innovative and beneficial solution. In short, the further development of abrasive composites will be driven by the concept of sustainable development, involving the improvement of functional properties while at the same time caring for the environment.

Acknowledgements

This work was supported by the National Science Centre Poland under research project no. UMO-2017/25/N/ST8/00401 and PUT research grant no. 03/32/DSPB/0806.

Conflict of interest

The authors declare no conflict of interest.

Author details

Artur Jamrozik, Łukasz Klapiszewski*, Beata Strzemiecka, Adam Voelkel and Teofil Jesionowski

*Address all correspondence to: lukasz.klapiszewski@put.poznan.pl

Faculty of Chemical Technology, Institute of Chemical Technology and Engineering, Poznan University of Technology, Poznan, Poland

References

[1] Malkin S, Guo C. Grinding Technology: Theory and Application of Machining with Abrasives. 2nd ed. New York: Industrial Press Inc.; 2008. ISBN-13: 978-0831132477

[2] Marinescu ID, Hitchiner M, Uhlmann E, Rowe WB, Inasaki I. Handbook of Machining with Grinding Wheels. 2nd ed. Boca Raton: CRC Press; 2016. ISBN: 9781482206685

[3] Bhushan B. Modern Tribology Handbook. Boca Raton: CRC Press; 2000. ISBN: 978084938 4035

[4] Jackson MJ, Davim JP. Machining with Abrasives. New York: Springer; 2011. ISBN: 978-1-4419-7302-3

[5] Gardziella A, Pilato LA, Knop A. Phenolic Resins: Chemistry, Applications, Standardization, Safety and Ecology. 2nd ed. Berlin: Springer; 2000. ISBN: 978-3-662-04101-7

[6] Jacobs FB. Abrasives and Abrasive Wheels, Their Nature, Manufacture and Use: A Complete Treatise on the Manufacture and Practical Use of Abrasives, Abrasive Wheels and Grinding Operations. London: Forgotten Books; 2017. ISBN-13: 978-0331571110

[7] Harris GL. Properties of Silicon Carbide. London: Inst of Engineering & Technology; 1995. ISBN-13: 978-0863415548

[8] Jayant Baliga B. Silicon Carbide Power Devices. London: World Scientific Pub. Co. Inc.; 2006. ISBN-13: 978-9812566058

[9] Yang D, Yu Y, Zhao X, Song Y, Lopez-Honorato E, Xiao P, Lai D. Fabrication of silicon carbide (SiC) coatings from pyrolysis of polycarbosilane/aluminum. Journal of Inorganic and Organometallic Polymers. 2011;**21**:534-540. DOI: 10.1007/s10904-011-9481-y

[10] Wellborn W. Modern abrasive recipes. Cutting Tool Engineering. 1994;**4**:42-47

[11] Linke B. Life Cycle and Sustainability of Abrasive Tools. Cham: Springer International Publishing; 2016. DOI: 10.1007/978-3-319-28346-3

[12] Field JE. The Properties of Diamond. London, New York: Academic Press; 1979. ISBN: 0122553500 9780122553509

[13] Field JE. Diamond—Properties and Definitions. Cambridge: Cavendish Laboratory; 1983

[14] Zaitsev AM. Optical Properties of Diamond—A Data Handbook. Berlin Heidelberg: Springer-Verlag; 2001. DOI: 10.1007/978-3-662-04548-0

[15] Bello I. Diamond and Cubic boron nitride: Synthesis and electronic applications. In: Proceedings of the Fourth International Conference on Advanced Semiconductor Devices and Microsystem "ASDAM '02"; 14–16 October 2002; Smolnice Castle, Slovakia: IEEE; 2002, p. 1-11

[16] Hitchiner MP, Wilks J. Some remarks on the chemical wear of diamond and CBN during turning and grinding. Wear. 1987;**114**:327-338. DOI: 10.1016/0043-1648(87)90120-7

[17] Bello I, Chong YM, Leung KM, Chan CY, Ma KL, Zhang WJ, Lee ST, Layyous A. Cubic boron nitride films for industrial applications. Diamond and Related Materials. 2005;**14**: 1784-1790. DOI: 10.1016/j.diamond.2005.09.003

[18] Souza Santos P, Souza Santos H, Toledo SP. Standard transition aluminas. Electron microscopy studies. Materials Research. 2000;**3**:104-114. DOI: 10.1590/S1516-14392000000400003

[19] US Patent US 80214492011

[20] Davies G. Charge states of the vacancy in diamond. Nature. 1977;**269**:498-500. DOI: 10.1038/269498a0

[21] Wakatsuki M. New catalysts for synthesis of diamond. Japanese Journal of Applied Physics. 1966;**5**:337-340. DOI: 10.1143/JJAP.5.337

[22] Akaishi M. New non metallic catalysts for the synthesis of high pressure, high temperature diamond. Diamond and Related Materials. 1993;**2**:183-189. DOI: 10.1016/0925-9635(93)90050-C

[23] Tong SL, Lin Z, Jiang X. CVD diamond films: Nucleation and growth. Materials Science & Engineering R: Reports. 1999;**25**:123-154. DOI: 10.1016/S0927-796X(99)00003-0

[24] Das D, Singh RN. A review of nucleation, growth and low temperature synthesis of diamond thin films. International Materials Review. 2007;**52**:29-64. DOI: 10.1179/174328007X160245

[25] Kamo M, Sato Y, Matsumoto S, Setaka N. Diamond synthesis from gas phase by decomposition of methane in microwave plasma. Journal of Crystal Growth. 1983;**62**:642-644. DOI: 10.1016/0022-0248(83)90411-6

[26] Kurihara K, Sasaki M, Kawanda M, Koshino N. High rate of synthesis of diamond by dc plasma jet chemical vapour deposition. Applied Physics Letters. 1988;**52**:437-438. DOI: 10.1063/1.99435

[27] Akatsuka F, Hirose Y, Komaki K. Rapid growth of diamond films using arc discharge technique. Japanese Journal of Applied Physics. 1988;**27**:L1600-L1602. DOI: 10.1143/JJAP.27.L1600

[28] Snail KA, Freitas JA, Vold CL, Hanssen LM. In: Proceedings of the 2nd International Symposium on Diamond Materials; May 1991; Washington, USA. Electrochemical Society; 1991. p. 91

[29] Snail KA, Vold CL, Marks CM, Freitas JA. High temperature epitaxy of diamond in turbulent flame. Diamond and Related Materials. 1992;**1**:180-186. DOI: 10.1016/0925-9635(92)90021-F

[30] Lin CR, Liao WH, Wei DH. Improvement on the synthesis technique of ultrananocrystalline diamond films by using microwave plasma jet chemical vapor deposition. Journal of Crystal Growth. 2011;**326**:212-217. DOI: 10.1016/j.jcrysgro.2011.01.100

[31] Vaitkuviene A, McDonald M, Vahidpour F. Impact of differently modified nanocrystalline diamond on the growth of neuroblastoma cells. New Biotechnology. 2015;**32**:7-12. DOI: 10.1016/j.nbt.2014.06.008

[32] Vikharev AL, Gorbachev AM, Kozlov AV. Microcrystalline diamond growth in presence of argon in millimeter-wave plasma-assisted CVD reactor. Diamond and Related Materials. 2008;**17**:1055-1061. DOI: 10.1016/j.diamond.2008.01.050

[33] Yang L, Jiang C, Guo S, Zhang L, Gao J, Peng J, Hu T, Wang L. Novel diamond films synthesis strategy: Methanol and argon atmosphere by microwave plasma CVD method without hydrogen. Nanoscale Research Letters. 2016;**11**:415-420. DOI: 10.1186/s11671-016-1628-x

[34] Sumiza H. Novel development of high-pressure synthetic diamonds "ultra-hard nanopolycrystalline diamonds". SEI Technical Review. 2012;**74**:15-22

[35] Vitrium3—White Paper [Internet]. 2016. Available from: http://www.saint-gobain-abrasives.com/en-us/resources/expertise/vitrium3-white-paper [Accessed: 2018-01-24]

[36] EPON™ Resin 160 produced by HexionTM, Technical Data Sheet [Internet]. Available from: http://www.hexion.com/en-US/product/epon-resin-160 [Accessed: 2018-01-13]

[37] Yoshida C, Okabe K, Yao T, Shiraishi N, Oya A. Preparation of carbon fibers from biomass-based phenol-formaldehyde resin. Journal of Materials Science. 2005;**40**:335-339. DOI: 10.1007/s10853-005-6087-1

[38] Srivastava R, Srivastava D. Studies on the synthesis and curing of thermosetting novolac resin using renewable resource material. International Journal of ChemTech Research. 2013;**5**:2575-2581

[39] Pilato LA. Phenolic Resins: A Century of Progress. Berlin: Springer; 2010. ISBN: 978-3-642-04714-5

[40] Silveira JVW, Bittencourt E, Aguila ZJ. Thermal and dynamic investigations on brake pad composites produced with lignin-phenolformaldehyde resin. Materials Science Forum. 2013;**730–732**:390-394. DOI: 10.4028/www.scientific.net/MSF.730-732.390

[41] Abarro GJ, Saake B, Lehnen R, Podschun J, Ishida H. Benzoxazines with enhanced thermal stability from phenolated organosolv lignin. RSC Advances. 2016;**6**:107689-107698. DOI: 10.1039/C6RA22334F

[42] Wypych G. Handbook of Fillers. 4th ed. Toronto: ChemTec Publishing; 2016 978-1-895198-91-1

[43] European Patent EP 2177318

[44] Jurga J, Voelkel A, Strzemiecka B. Application of different analytical methods used in the study of the cross-linking of resins in intermediate-product used in manufacturing of abrasive articles. Journal of Applied Polymer Science. 2009;**112**:3305-3312. DOI: 10.1002/app.29840

[45] Laza JM, Alonso J, Vilas JL, Rodríguez M, León LM, Gondra K. Influence of fillers on the properties of a phenolic resin cured in acidic medium. Journal of Applied Polymer Science. 2008;**108**:387-392. DOI: 10.1002/app.26816

[46] Strzemiecka B, Heberger K, Voelkel A. Similarity and grouping of perlite and zeolite abrasive fillers: A replacement test. Journal of Applied Polymer Science. 2013;**127**:3839-3847. DOI: 10.1002/app.37695

[47] Strzemiecka B, Voelkel A, Chmielewska D, Sterzyński T. Influence of different fillers on phenolic resin abrasive composites. Comparison of inverse gas chromatographic and dynamic mechanical-thermal analysis characteristics. International Journal of Adhesion and Adhesives. 2014;**51**:81-86. DOI: 10.1016/j.ijadhadh.2014.02.013

[48] Strzemiecka B, Voelkel A, Hinz M, Rogozik M. Application of inverse gas chromatography in physicochemical characterization of phenolic resin adhesives. Journal of Chromatography. A. 2014;**1368**:199-203. DOI: 10.1016/j.chroma.2014.09.069

[49] Strzemiecka B, Kołodziejek J, Kasperkowiak M, Voelkel A. Influence of relative humidity on the properties of examined materials by means of inverse gas chromatography. Journal of Chromatography. A. 2013;**1271**:201-206. DOI: 10.1016/j.chroma.2012.11.037

[50] Biermann CJ. Handbook of Pulping and Papermaking. 2nd ed. London: Academic Press; 1996. ISBN: 978-0-12-097362-0

[51] El Mansouri N-E, Pizzi A, Salvado J. Lignin-based wood panel adhesives without formaldehyde. Holz als Roh- und Werkstoff. 2007;**65**:65-70. DOI: 10.1007/s00107-006-0130-z

[52] Klapiszewski Ł, Jamrozik A, Strzemiecka B, Matykiewicz D, Voelkel A, Jesionowski T. Activation of magnesium lignosulfonate and kraft lignin: Influence on the properties of phenolic resin-based composites for potential applications in abrasive materials. International Journal of Molecular Sciences. 2017;**18**:1224-1243. DOI: 10.3390/ijms18061224

[53] Klapiszewski Ł, Jamrozik A, Strzemiecka B, Borek B, Matykiewicz D, Voelkel A, Koltsov I, Jesionowski T. Characteristics of multifunctional, eco-friendly lignin-Al_2O_3 hybrid fillers and their influence on the properties of composites for abrasive tools. Molecules. 2017;**22**:1920-1939. DOI: 10.3390/molecules22111920

IntechOpen

Chapter 7

Tuning the Morphology and Surface Property of Mineral Particles by Grinding Media

Zhiyong Gao and Chengwei Li

Additional information is available at the end of the chapter

http://dx.doi.org/10.5772/intechopen.74836

Abstract

Grinding of minerals for particle size reduction and liberation is a prerequisite for successful mineral flotation separation and powder modification. Different grinding media produce mineral particles with different physical morphology and surface chemistry properties. Different mill particles expose different proportions of cleavage surfaces which lead to different shape indexes and different surface reactivities to organics, such as collector. Rod mill produces scheelite particles with a higher exposure of more reactive {101} surface that are beneficial for a stronger interaction with collector. More exposure of {101} surface also causes the rod mill particles to possess such values as larger elongation and flatness that are essential for particles attachment to air bubbles by shortening the induction time. The rod mill particles have a lower critical surface tension, greater hydrophobicity and a better flotation recovery when treated with the collector. In addition, the rod mill particles with a narrow particle size distribution have a smaller specific surface area, so the full monolayer adsorption of the collector on their surfaces can be achieved at a relatively lower concentration. These findings will help establish the relation between the particle surface physicochemistry and wettability, hence providing valuable guidance for the optimization of flotation separation and powder modification technology.

Keywords: grinding media, morphology, wettability, reactivity, flotation, surface modification, scheelite

1. Introduction

Size reduction by mechanical comminution (i.e., crushing and grinding) is an indispensable process in many fields, such as the field of mineral processing, metallurgical, power and chemical industries [1], etc. However, this process consumes such a considerable amount of energy that it becomes the heaviest energy consumption unit in many industries [2]. For

example, in the field of mineral processing, comminution of run-of-mine consumes 70% of the total energy [3]. Therefore, optimizing the process of crushing and grinding is of great significance for achieving energy-saving and cost-reducing in minerals processing.

Mineral processing is a predominant technology used to fulfill the enrichment of valuable minerals from coexisted (undesired) gangue minerals and then, provides raw materials for the following metallurgical operation [4]. During this process, minerals first go through crushing and grinding for particle size reduction and sufficient mineral liberation before separation operations [5, 6]. Conventionally speaking, there are primarily two ways for separation: gravity separation and flotation separation. Gravity separation is used when both the valuable minerals and gangues are coarsely grained in ore deposits and the density between them features a significant distinction. In this process, the rod mill is commonly employed to break preferentially coarser particles, produce more uniform particle products and avoid overgrinding [7–9]. In gravity separation, the valuable minerals and gangues have different movement speeds and trajectories in the equipment, such as jigging, dense medium cyclone and centrifuge, thus leading to the successful separation. But with the ever increasing demands for processing the low-grade, fine-grained and disseminated ores, the flotation separation has been increasingly employed as a complementary or substitute method for gravity separation [10]. Flotation is a separation method based on the differences in wettability at particle surfaces after being treated with surfactants, during which sufficient liberation of the fine-grained minerals is the key factor for a successful separation. Compared with the rod mill under the same energy consumption, the ball mill is more beneficial for the production of finer particle products [11].

Different grinding methods possess different breakage mechanisms and accordingly, produce particles with different shapes or morphologies [12]. For the rod mill, line loads are exerted on the mineral particles, and the predominant breaking forces are the impact which can produce particles with sharp edges [13]. In contrast, the ball mill imposes point loads on the particles, so that the main forces are abrasion and chipping which can trim off the corners and sharp edges of particles efficiently [14, 15]. Mill particles with different shapes always exhibit different gravity or flotation behavior. The research group led by Yekeler from Cumhuriyet University found that compared with the ball mill particles, the rod mill ones provide a more elongated and smoother surface, thus performing a better floatability [16–19]. This phenomenon can be explained by the higher attachment efficiency of the elongated particle to the air bubbles through accelerating the rupture of the surrounding liquid film and shortening the induction time [20, 21]. Recently, Xia [22] has systematically reviewed the role of particle shape in mineral floatability, and concluded that the particles with shape far away from sphere own an increasing surface hydrophobicity and floatability. Moreover, the coverage of collector on irregular particle surface is conducive to the stability of the three-phrase contact line and hence increasing the flotation recovery.

The grinding environments also play a considerable role on the surface properties and flotation behavior of the ground particles. Feng and Alrichv [23] indicated that more micro - structural defects found in the dry ground samples can serve as the active sites to accelerate the adsorption of collector, while smoother and cleaner surfaces are found in the wet mill particles. Recently, the spodumene samples were also ground using dry and wet mills by Zhu

et al. [24] and Xu et al. [25]. The separate research groups independently found that more {110} and {100} surfaces are exposed for the wet mill particles while more {010} exposed for the dry mill ones. The wet mill particles are more hydrophobic when treated with collector and accordingly, obtain a better flotation recovery.

Scheelite $CaWO_4$ is the most prominent mineral source for tungsten which is of great importance in many other fields like electronic information, aerospace and military [26]. The above two separation methods have been used to enrich the scheelite from gangue minerals for a long time [27–29]. In Xingluokeng Tungsten Ore (Fujian, China), the ore deposit mainly belongs to the scheelite-feldspar-quartz type. Because of the coarsely grained characteristics and distinct density differences between scheelite and gangues, the rod mill has been employed to achieve mineral liberation prior to the gravity separation. However, with the continuous consumption of the high-grade ore, the scheelite has become much more fine-grained. Thus, the gravity separation was proved to be less efficient in recent years, and a regrinding-flotation process after gravity separation was investigated to improve the comprehensive recovery of scheelite.

Unlike the Xingluokeng ore, the scheelite deposit in Shizhuyuan Ore (Hunan, China) mainly belongs to the scheelite-calcite-fluorite-grossularite type with a very fine-grained characteristic. Furthermore, due to the similar specific gravity between sheelite and grossularite, and similar physicochemical properties between scheelite and calcite and fluorite [30], the flotation method is therefore, the dominant process to recover the sheelite. Naturally, the ball mill is used to liberate the scheelite particles [31].

In the past 2 years, our group prepared a novel metal-organic complex, i.e., lead- benzohydroxamic acid (BHA) complex. This complex, as a collector, was successfully applied to the selective flotation of scheelite from gangues in Shizhuyuan Ore, leading to a significant increase in the comprehensive recovery of WO_3 by 8-10% [32, 33]. However, when we used this complex in Xingluokeng Ore, some obvious differences in the flotation behavior and recovery of scheelite were observed compared with those in Shizhuyuan Ore. We thought that the differences were mainly caused by the different mill media and ore type.

In this chapter, the surface properties and flotation behavior of scheelite particles produced by ball and rod mills were studied through single mineral flotation experiment, scanning electron microscopy (SEM) observation, wettability measurement, and X-ray diffraction (XRD) test. These results will help establish the relation between the particle surface properties and the grinding media, hence providing guidance for optimizing flotation separation.

2. Experimental procedures

2.1. Materials and reagents

Representative samples of pure scheelite crystals were collected from the Huili mine, Sichuan, China. The chemical analysis of samples confirmed that the scheelite samples were over 98% pure.

Chemically pure benzohydroxamic acid (BHA) (above 98% purity) was purchased from Tokyo Chemical Industry. Lead nitrate with 99% purity was purchased from Tianjin Kermil Chemical Reagents. The pH of solution was adjusted with sodium hydroxide (NaOH) or hydrochloric acid (HCl) stock solutions. Deionized (DI) water with a resistivity of over 18 MΩ × cm was used throughout the experiments.

2.2. Methods

2.2.1. Grinding tests

Representative samples of pure scheelite crystal samples (**Figure 1a**) were first crushed from a diameter of 40–5 mm using the JC6 jaw crusher (Beijing Grinder Instrument Equipment Co., Ltd.). Then the crushed samples were ground by ball and rod mills. The grinding tests were operated using the 146 × 200 mm laboratory size mill (**Figure 1b**).

For the ball mill, corundum balls with diameters of 21, 16 and 12 mm were used as grinding media. For the rod mill, corundum rods of 15 and 11 mm in diameter and 15 cm in length were used. Scheelite samples with a total mass of 200 g were fed into the mill and ground for 30 s each run to prevent over-grinding. After a run, the ground products were sieved by a standard screen with a pore size of 74 μm (200 mesh). The oversize particles were returned to the mill for

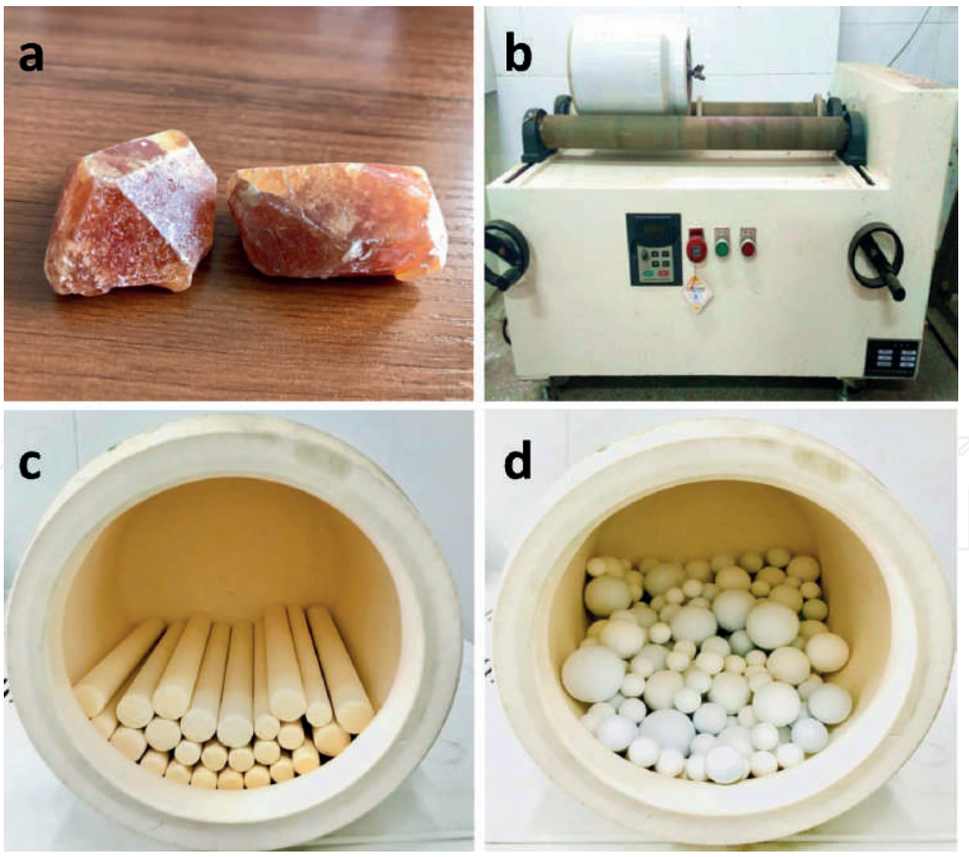

Figure 1. (a) Pure scheelite crystal samples, (b) grinder, (c) corundum rod media, and (d) corundum ball media used in the grinding tests.

the next run, while the products under the screen were collected for further sieving to obtain particles in the size fraction of −74 + 38 μm (the size of the particle is between 38 and 74 μm). The samples with required size were rinsed with Deionized (DI) water and dried at the temperature of 60°C. The surface area measurement (BET) indicated that the special surface areas of the ball and rod mill particles are 0.040 and 0.027 m^2/g, respectively.

2.2.2. Particle shape characterization by SEM

The shape characterization of milled particles was imaged by the JSM-6490LV SEM instrument. Assuming that the projection of the particles had the ellipse-like shape [17], the imaged micrographs were analyzed using CorelDraw×4 software to measure the length (L) and width (W) of the particles. As shown in **Figure 2**, the particles without overlapping nor border out of the picture were chosen. For each particle, the mean value of the five liner lengths and widths were taken as the real length (L) and width (W), respectively [16, 17]. Then more than 200 particles were measured and the L and W of the particle groups were calculated by averaging all value of the chosen particles.

Based on the ellipse-like shape assumption, Eqs. (1) and (2) were used to calculate the area (A) and perimeter (P), respectively.

$$A \approx \frac{\pi LW}{4} \tag{1}$$

$$P \approx \frac{1}{2}\pi\left[\frac{3}{2}(L+W) - (LW)^{1/2}\right] \tag{2}$$

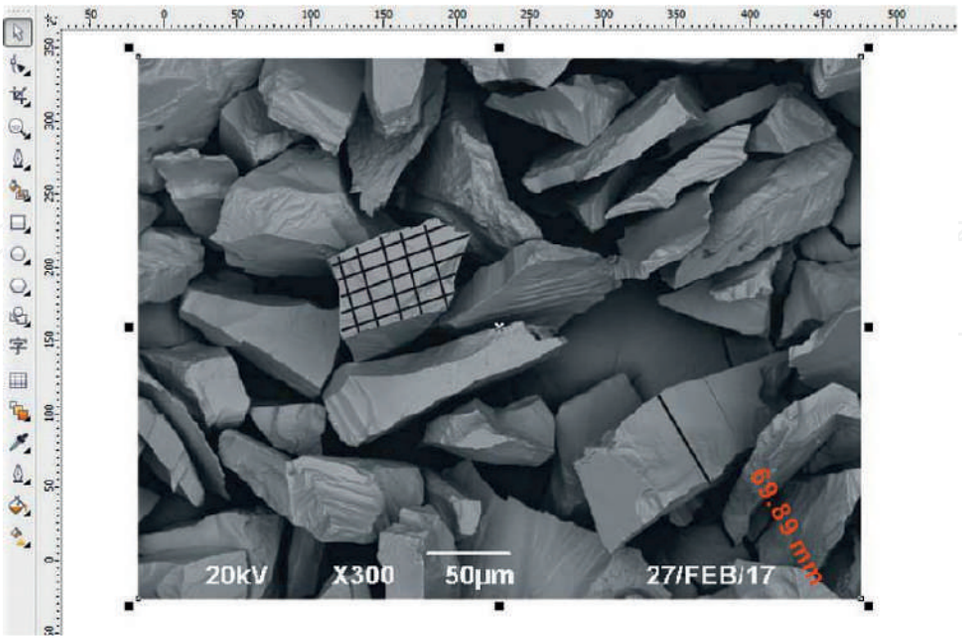

Figure 2. Measurements of the length (L) and width (W) of a particle projection exported from an SEM micrograph on CorelDraw software.

With the values of L, W, A and P, the four shape factors, namely the roundness (Ro), flatness (F), elongation (E) and relative width (RW), were calculated using Eqs. (3)–(6).

$$\mathrm{Ro} = \frac{4\pi \mathrm{A}}{\mathrm{P}^2} \tag{3}$$

$$\mathrm{F} = \frac{\mathrm{P}^2}{4\pi \mathrm{A}} \tag{4}$$

$$\mathrm{E} = \frac{\mathrm{L}}{\mathrm{W}} \tag{5}$$

$$\mathrm{RW} = \frac{\mathrm{W}}{\mathrm{L}} \tag{6}$$

It should be noted that the maximum value of the roundness is 1.0 for a circle, while the flatness has a minimum of 1.0 for a circle.

2.2.3. X-ray diffraction (XRD) measurement

X-ray diffractometer (D8-ADVANCE Bruker-AKS) was run in the reflection mode with Cu Kαradiation (λ = 1.5406, tube potential of 40 mV, and tube current of 40 mA), and at a goniometer speed of 4°/min. It is important that the samples were randomly oriented during the sample preparation process.

2.2.4. Wettability measurement

To measure the wettability of nubby samples, the sessile drop technique [34] and the captive bubble method [35] have been widely used, while as for powder samples, the Washburn method [36] and the flotation method [37] were employed. In this study, the flotation method was employed to investigate the wettability of the milled particles treated by the activator and collector. This method is based on the assumption that the flotation recovery of the minerals decreases with the decrease in the surface tension (γ) of the solution [38]. Therefore, methanol solution with different concentrations were used as the flotation media and 2.0 g of samples was conditioned by 1×10^{-4} mol/L lead nitrate and 1×10^{-4} mol/L BHA. After 3 min of flotation at pH 9 (an industrially preferred pH for effective scheelite flotation), the froth concentrates and tailings were filtered, dried and weighted to calculate the flotation recovery.

Moreover, the advancing contact angle of the commonly exposed cleavage surfaces of scheelite (the {101} and {001} surfaces) was measured by the sessile-drop technology using a goniometer (GBX, France) at 20°C and ambient relative humidity of about 50%. The accuracy of the measurements was approximately ±2°. Firstly, and the prepared sample surfaces were immersed in the surfactant solution with desired concentration under gentle agitation for 30 min, then gently washed with distilled water and vacuum dried at 50°C for 15 min. Then a water drop of about 3.5 μL was placed on the sample surface and the readings of contact angles were taken automatically on the left and right sides of the water droplet profile by computer software. The height of the drop is dependent on the wettability of the scheelite

sample surface. Ten readings of contact angle were taken on each drop within 1 min after placing the drop, and the contact angle commonly reaches a stationary value (the equilibrium contact angle) after 30 s. At least three drops were measured and the mean value was taken as the real advancing contact angel for each crystal surface after treated with a certain concentration of collector [39–41].

2.2.5. Micro-flotation test

Micro-flotation tests were carried out in an XFG flotation machine with a 40 mL plexiglass cell, at an impeller speed of 1650 rpm. The mineral suspension was prepared by adding 2.0 g of minerals and 36 mL DI water into the flotation cell and agitated for 2 min, followed by the adjustment of pH using NaOH or HCl for 2 min. Then the reagents were added in following orders: (1) the lead nitrate as the activator (2) the BHA as the collector; (3) 25 μL/L (i.e., adding 25 μL frother into 1 L mineral suspension) terpineol as the frother. Once the desired reagent was added, the suspension was agitated for 3 min. The stable pH value was recorded before the flotation. The flotation process lasted for 3 min before the flotation products were collected, filtered, dried and weighted. The flotation recovery was calculated using the weight of the dry products.

3. Results and discussions

3.1. Shape indexes of scheelite particles by different mills

The shape characterization of both the ball and rod mill particles was determined using 2D shape analysis (SEM method), and the mean values of the main shape indexes calculated according to Eqs. (1)–(6) are listed in **Table 1**. In addition, the distribution of the roundness and the elongation were calculated and shown in **Figure 3**.

Furthermore, the Statistical Product and Service Solutions (SPSS) software and the "two-sample t-test" were applied to the study of shape index (flatness, roundness, elongation and relative width) differences of the products produced by the ball and rod mills. The values of the shape indexes were compared pair-wise for any statistically significant differences at the 95% confidence interval with the results listed in **Table 1**.

As shown in **Table 1**, the rod mill particles have higher values of elongation (E) and flatness (F), while the ball mill particles possess larger values of roundness (R) and relative width (RW). Since all values at the column of "Sig. (2-side)" listed in **Table 2** are less than 0.05, a significant difference between the ball and rod mill scheelite products with a confidence interval of 95% is

Mill products	Particle number	L(μm)	W(μm)	A(μm^2)	P(μm)	E	F	Ro	RW
Ball	240	96.140	63.830	4817.244	253.741	1.505	1.069	0.935	0.664
Rod	240	108.867	67.412	5796.279	281.199	1.615	1.097	0.916	0.623

Table 1. Mean values of the shape indexes of both the ball and rod mill products of the scheelite mineral.

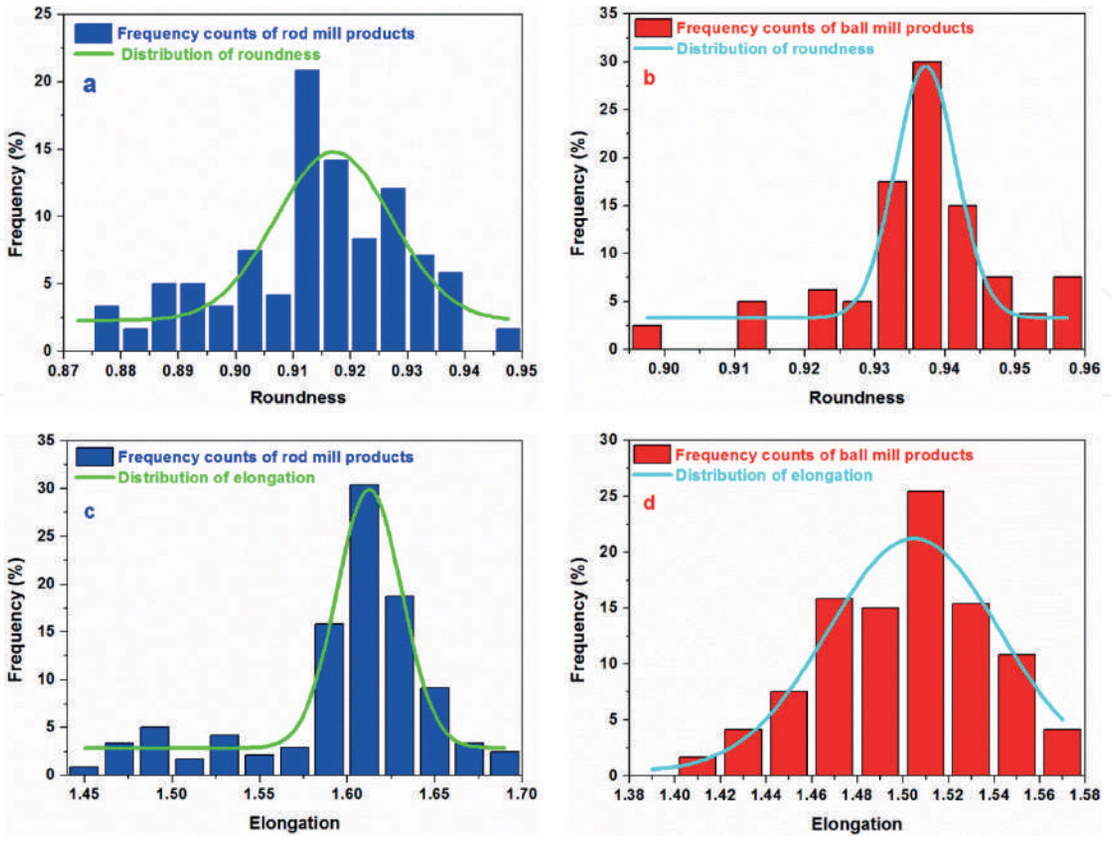

Figure 3. The distribution of shape indexes: The roundness of the (a) rod mill and (b) ball mill products, the elongation of the (c) rod mill and (d) ball mill products.

Parameter	Pair differences							
	Mean	Standard deviation	Standard error of mean	95% Confidence interval of the difference		t	df	Sig.(2-side)
				Lower	Upper			
F_d	0.02648	0.02363	0.00673	0.01614	0.03873	17.359	239	0.000
R_d	−0.02291	0.01986	0.00464	−0.0301	−0.0118	−17.555	239	0.000
E_d	0.10053	0.02021	0.00483	0.05160	0.14945	76.444	239	0.000
RW_d	−0.04127	0.00750	0.00222	−0.04910	−0.00886	−85.232	239	0.005

L_d, W_d, F_d, R_d, E_d and RW_d represent the shape differences of the scheelite particles produced by rod and ball mills.

Table 2. The statistical shape differences of the ball and rod mill products determined by the two-sample t-test.

inferred [42]. It was noted from the literature that the 2D shape data is used to reproduce the crucial shape characteristics of the real 3D shape indexes when the measured particles number is greater than 200 [43–47]. Therefore it is worth mentioning here that the shape indexes obtained in this study are reliable.

http://dx.doi.org/10.5772/intechopen.74836

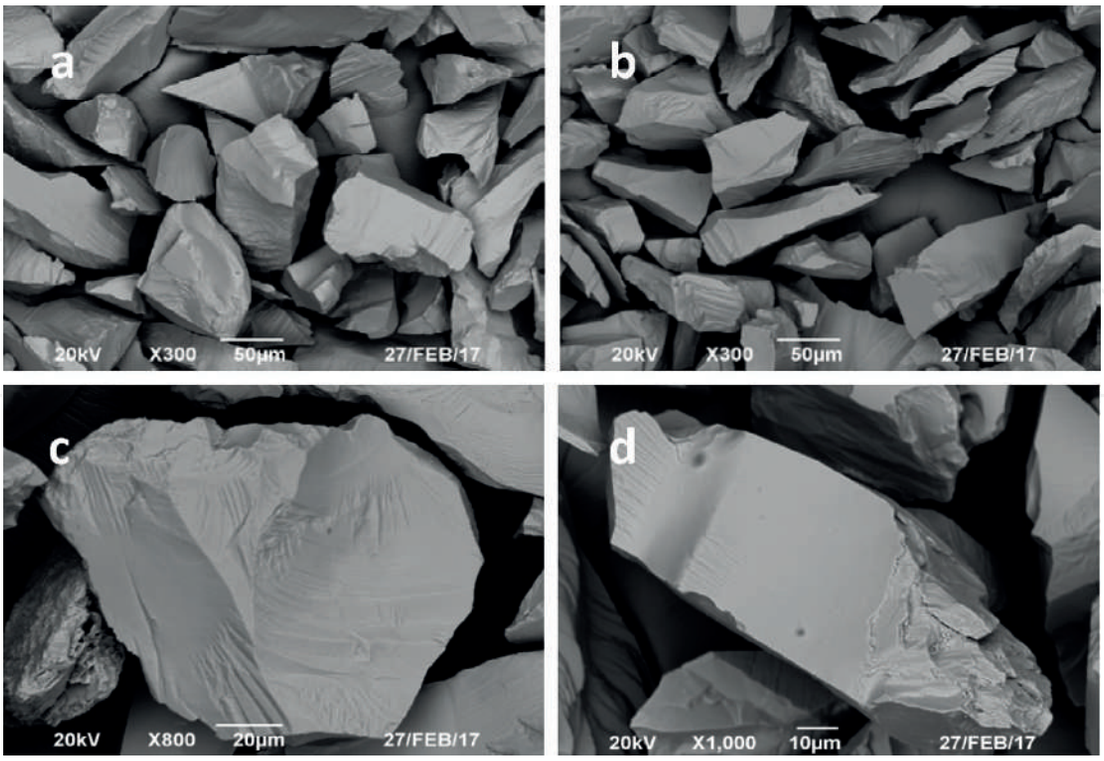

Figure 4. SEM pictures of the ball (a,c) and rod (b,d) mill particles of scheelite mineral.

SEM pictures in **Figure 4** show that the ball mill particles are more rounded while the rod mill particles are more elongated with more sharp edges. Those differences in the shape indexes between the ball and rod mill particles could be explained by the fact that breakage mechanism determines particle shape in all comminution equipment. The rod mill exercises line loads on the particles and the dominant breakage mechanism is the impact, during which the sharp edges are created, turning the particle to become more elongated [13]. Whereas the ball mill exerts point loads on the particles, and the predominant breaking forces are abrasion and chipping, which could eliminate the corners and sharp edges of the particles, turning them to become more rounded [14, 15].

3.2. XRD measurement results

Previous literatures reported that the relative exposure proportion of different crystal surfaces changes when the grinding environment varied [24, 25]. Previous publications revealed that the exposure of crystal surfaces of scheelite particles follows the order {112}, {101} and {001} [48–51]. The schematic of the commonly exposed surfaces of scheelite crystal particles can be found in **Figure 5**. In this work, the XRD measurements were conducted to investigate the exposure of different crystal surfaces in the two mill products, and the results are shown in **Figure 6**.

The relative intensity of a maxima (or peak) in the spectrum is believed to represent the relative exposure proportion of the crystal surfaces in the particulate samples [52, 53]. **Figure 6**

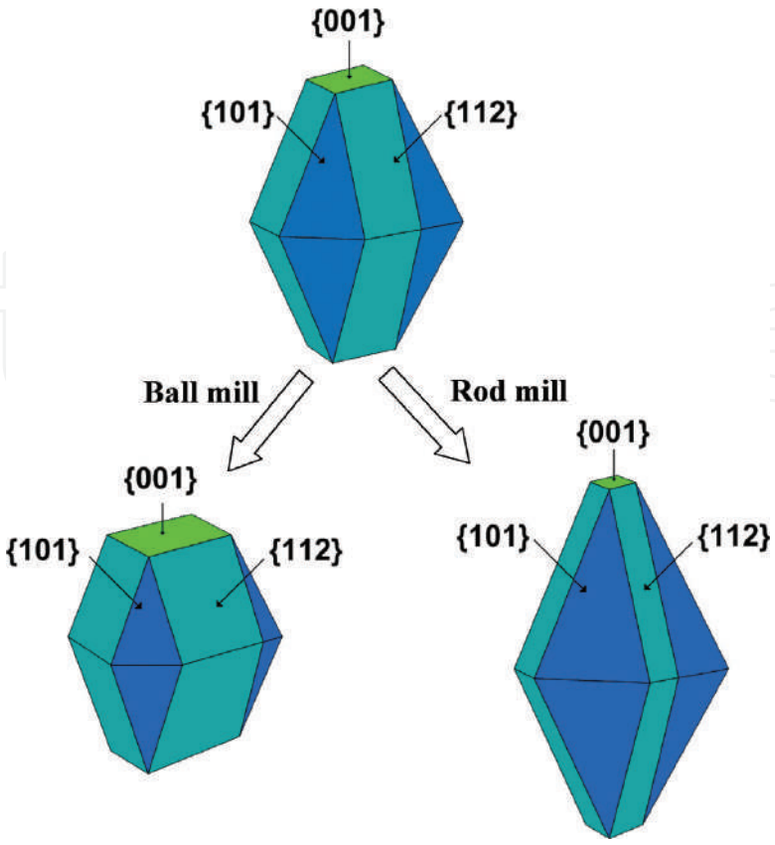

Figure 5. The schematic of the commonly exposed surfaces of original, ball and rod milled scheelite particles.

shows the same trend of the exposure of three main crystal surfaces of scheelite as **Figure 5**. Moreover, the {112} surface is the most abundant plane, and the intensity of the {112} surface is nearly the same for both mill products. In this case, the exposure proportion of {112} surface in the mill products is assumed as 100%. Accordingly, the relative proportions of the {101} plane in ball and rod mill samples are calculated to be 71.9% and 87.7%, respectively, while for the {001} planes, 44.4% and 33.8% respectively. The ball mill samples expose more {001} surfaces while the rod mill samples show more {101} surfaces. It is also interesting to mention that, from the **Figure 5**, more exposure of {001} surfaces will lead to the decrease in the elongation and the increase in the roundness of scheelite particles, while more exposure of {101} surface will increase the elongation and reduce the roundness of scheelite particles. That is to say, ball mill particles with more {001} surfaces are of a higher Ro value smaller E value which was verified by the results in **Table 1**.

It has been reported that every Ca atom on the scheelite {101} surface is fivefold-coordinated, while Ca on the {001} surface is sixfold-coordinated, as shown in **Figure 7**. The Ca atom in bulk scheelite crystal is eightfold-coordinated to surrounding oxygens. Based on our early findings [40, 54] that the atom with more dangling bonds is more active, the Ca atom on the {101} surface is more active than that on {001} surface, and has a higher interaction strength with organics, such as oleate. The atomic simulation results showed that a larger adsorption energy

http://dx.doi.org/10.5772/intechopen.74836

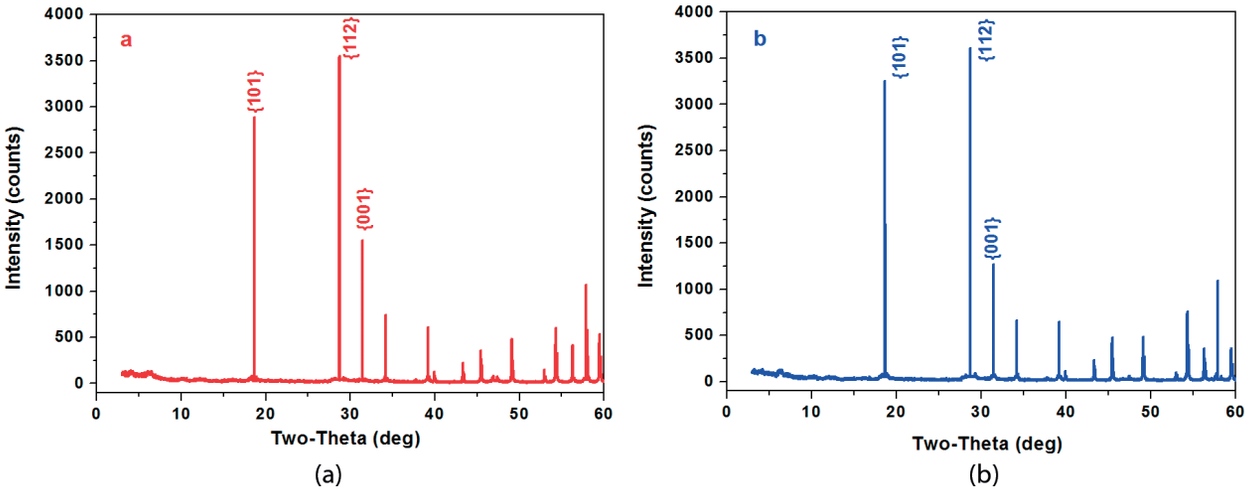

Figure 6. The XRD spectrums of the (a) ball and (b) rod mill products of scheelite minerals.

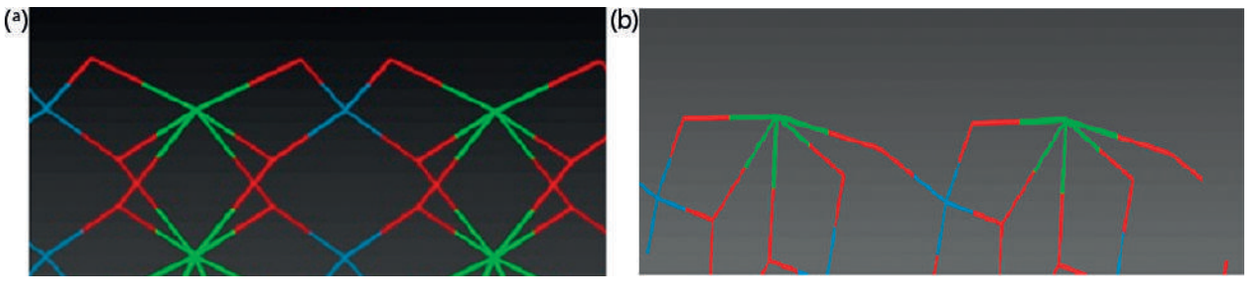

Figure 7. The bonding state of the top layer of scheelite (a) {001} and (b) {101} surfaces (green-Ca, red-O, and blue-W).

(−102 kJ/mol) of the oleate on the {101} surface was calculated while the adsorption energy was −93 kJ/mol for the oleate on the {001} surface [10]. Thus, it is tenable to infer that the rod mill products with relatively more {101} surface have stronger interaction with the collector and may possess a higher flotation recovery.

3.3. Wettability test results

The flotation method was used to investigate the wettability of both ball and rod mill particles. The experiments were conducted at pH 9 using 1×10^{-4} mol/L lead nitrate as the activator and 1×10^{-4} mol/L BHA as the collector at different concentration of the methanol solution. The critical surface tension (γ_c) of wetting was determined by plotting the percent recovery (R%) versus the surface tension of the methanol - water solutions (γ_{LA}), which gives a recovery R % = 0 at $\gamma_c = \gamma_{LA}$. The particles are wetted and cannot float when $\gamma_{LA} < \gamma_c$, indicating that the mineral with a lower γ_c is more hydrophobic [55]. The γ_{LA} of the methanol solution was measured by the Automatic Surface Tensiometer and the results are provided in **Figure 8**. And the flotation results are shown in **Figure 9**. It shows that the γ_c of the ball and rod mill

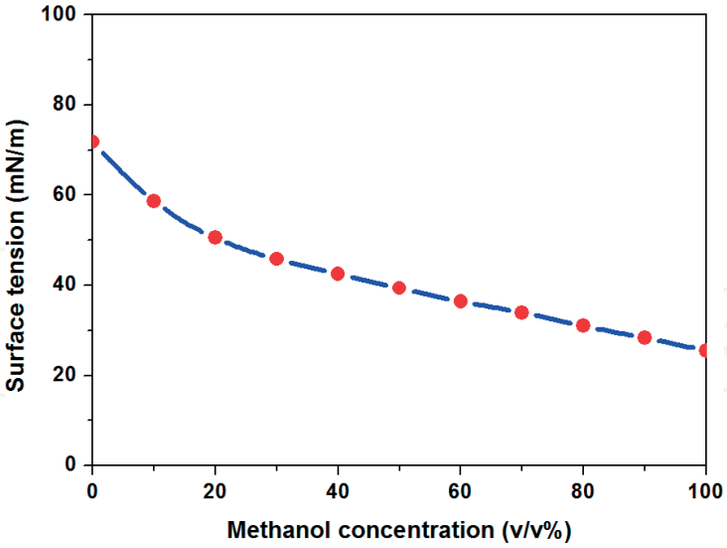

Figure 8. Variation of the surface tension of the methanol – water solutions (γ_{LA}) with the increase of mechanol concentration.

particles are approximately 43 and 41 mN/m, respectively, indicating that the ball mill ones are more likely to be wetted while the rod mill ones are more hydrophobic, which may result in a higher floatability.

According to the XRD measurement results, in addition to {112} surface, the ball mill samples expose more {001} surfaces while the rod mill samples show more {101} surfaces, which means that the wettability of the ground particles may be influenced by the proportion of the exposed surfaces. Then the advancing contact angles of both the {001} and {101} crystal planes treated by the lead nitrate and the BHA were measured, and the results are shown in **Figure 10**. It demonstrates that the scheelite {101} surface has higher contact angles after being treated with the surfactants, meaning that {101} is more hydrophobic than {001} surface.

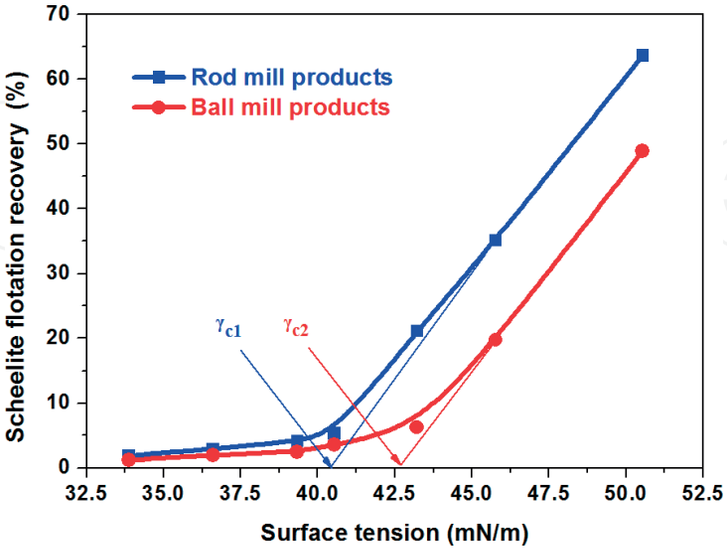

Figure 9. Flotation recoveries of the ball and rod mill products as a function of the methanol surface tension. ($C_{Lead\ nitrate} = 1 \times 10^{-4}$ mol/L; $C_{BHA} = 1 \times 10^{-4}$ mol/L; $C_{Terpineol} = 25$ μL/L; pH = 9 ± 0.2).

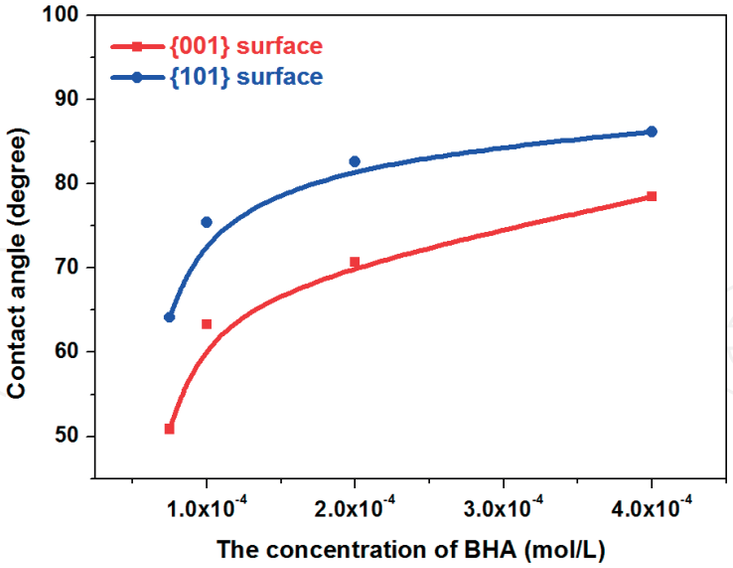

Figure 10. Contact angles of the scheelite (a) {101} and (b) {001} crystal surfaces. ($C_{Lead\ nitrate} = 1 \times 10^{-4}$ mol/L; pH = 9 ± 0.2).

From the above measurements, it can be concluded that the rod mill particles with more {101} surfaces exposed and a lower critical surface tension were more hydrophobic. As a result, the differences in wettability could influence the flotation behavior of these two different mill particles.

3.4. Micro-flotation experiment results

Micro-flotation experiments were conducted to study the flotability of the particles in the fraction of −74 + 38 μm that ground by the ball and rod mills. The flotation results, using different concentrations of BHA as collector at a pH of 9 ± 0.2, are provided in **Figure 11**. **Figure 11** shows that both the ball and rod mill particles have a similar trend of flotation

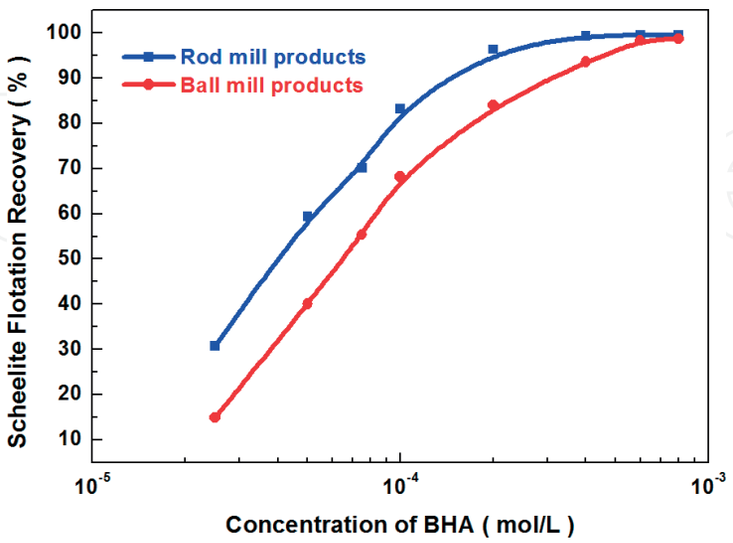

Figure 11. Flotation recoveries of the ball and rod mill products as a function of the BHA concentration. ($C_{Lead\ nitrate} = 1 \times 10^{-4}$ mol/L; $C_{Terpineol}$ = 25 μL/L; pH = 9 ± 0.2).

recovery. The flotation recovery increases steadily with the increasing of BHA concentration till it reaches 4×10^{-4} mol/L for the rod mill particles and 6×10^{-4} mol/L for the ball mill ones, where the maximum recovery for both two samples are obtained at given concentrations of BHA, respectively. The maximum recovery may be caused by the monolayer adsorption of collector on the scheelite surfaces [56]. For the rod mill samples, it is easier to reach the monolayer adsorption because of the smaller specific surface area of 0.027 m^2/g compared with that of 0.040 m^2/g for the ball mill ones. Moreover, the flotation results, obtained at a pH of 6–11 are demonstrated in **Figure 12**. **Figure 12** shows that the recoveries of both milled particles follow a similar trend, but a higher recovery for the rod mill particles was observed. It was also observed that the flotation recovery increases with the increasing pH of solution until it reaches the value of 9, where the maximum recovery is achieved for both milled particles [32].

Therefore, it can be inferred from the micro-flotation results that the flotation behavior of the ball and rod mill particles is similar, while the rod mill ones have a better flotation performance than the ball mill ones. And the reason could be explained by the shape and the surface chemistry differences of scheelite particles ground by ball and rod mills. To begin with, the rod mill particles expose more {101} surfaces, on which the Ca sites are more reactive, resulting in a stronger interaction of collector with the rod mill particles and a better floatation performance. In addition, the wettability measurements show that the ball mill scheelite, with higher critical surface tension and more {001} surfaces, may have relatively lower contact angles and may be more likely to get wetted during the flotation process. Secondly, the rod mill particles, with a lower specific area and larger elongation, are more easily attached to the air bubbles than the rounded ones. This can be attributed to the sharp edges of elongated particles, which are conducive for rupturing the water film at the mineral/solution interface and help shorten the attachment time, leading to the improvement of the collision efficiency and flotation recovery.

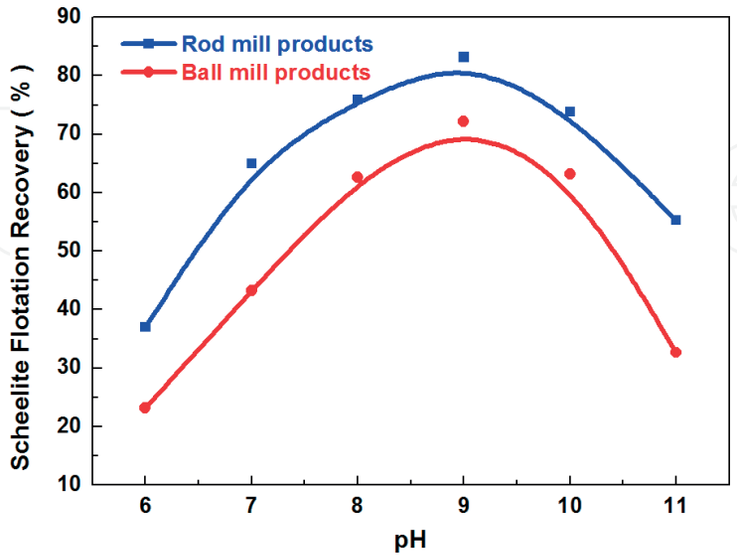

Figure 12. Flotation recoveries of the ball and rod mill products as a function of the solution pH. ($C_{Lead\ nitrate} = 1 \times 10^{-4}$ mol/L; $C_{BHA} = 1 \times 10^{-4}$ mol/L; $C_{Terpineol} = 25$ μl/L).

http://dx.doi.org/10.5772/intechopen.74836

4. Conclusions

In this work, the morphology and the surface properties of the scheelite particles with a size of −74 + 38 μm produced by ball and rod mills were studied through SEM observation, XRD analysis, wettability measurement, and single mineral flotation experiment. The flotation results revealed that the rod mill particles are much easier to achieve a monolayer adsorption of collector and hence have a higher flotation recovery compared to the ball mill ones which can be explained from both physical and chemical points of view. The XRD spectrums showed that minerals particles obtained from ball and rod mill have similar expose intensity of abundant {112} surface. However, the rod mill particles have more {101} surface exposed with more reactive Ca atoms while more {001} surface is exposed for the ball mill particles. Moreover, more exposure of {001} surfaces will lead to the decrease in the elongation and the increase in the roundness of scheelite ball mill particles, while more exposure of {101} surface will increase the elongation and reduce the roundness of scheelite rod mill particles. Those discussions were verified by the SEM observations and shape indexes distribution calculation. The contact angles of {101} surface are larger than that of the {001} surface after being treated with the collector, indicating that the rod mill particles with more exposed {101} surfaces possess a higher hydrophobicity. The wettability measurements indicated that the values of the critical surface tension (γ_c, a measure of surface tension) are 41 and 43 mN/m for the rod and ball mill particles treated with collector, respectively. The rod mill particles with more exposure of reactive {101} surfaces and higher elongation have stronger attachment to collectors and air bubbles, and hence a higher hydrophobicity and flotation recovery in the presence of collector.

Acknowledgements

The authors acknowledge the financial support from the National Natural Science Foundation of China (51774328, 51404300), the Young Elite Scientists Sponsorship Program by CAST(2017QNRC001), the Innovation-driven Program of Central South University of China (2017CX007), the Key Program for International S & T Cooperation Projects of China (2016YFE0101300), and the National 111 Project (B14034), the Innovation Program for Postgraduate Students of Central South University (2017zzts576). Natural Science Foundation of Hunan Province of China (2018JJ2520).

Author details

Zhiyong Gao* and Chengwei Li

*Address all correspondence to: zhiyong.gao@csu.edu.cn

School of Mineral Processing and Bioengineering, Central South University, Changsha, Hunan, China

References

[1] Kursun H, Ulusoy U. Influence of shape characteristics of talc mineral on the column flotation behavior. International Journal of Mineral Processing. 2006;**78**:262-268. DOI: 10.1016/j.minpro.2005.11.003

[2] Ballantyne GR, Powell MS. Benchmarking comminution energy consumption for the processing of copper and gold ores. Minerals Engineering. 2014;**65**:109-114. DOI: 10.1016/j.mineng.2014.05.017

[3] Curry JA, Ismay MJL, Jameson GJ. Mine operating costs and the potential impacts of energy and grinding. Minerals Engineering. 2014;**56**:70-80. DOI: 10.1016/j.mineng.2013.10.020

[4] Austin LG, Trass O. Size reduction of solids crushing and grinding equipment. In: Fayed ME, Otten L, editors. Handbook of Powder Science & Technology. Boston, MA: Springer US; 1997. pp. 586-634

[5] Leroy S, Dislaire G, Bastin D, Pirard E. Optical analysis of particle size and chromite liberation from pulp samples of a UG2 ore regrinding circuit. Minerals Engineering. 2011;**24**:1340-1347. DOI: 10.1016/j.mineng.2011.06.006

[6] Bournival G, Ata S, Wanless EJ. The roles of particles in multiphase processes: Particles on bubble surfaces. Advances in Colloid and Interface Science. 2015;**225**:114-133. DOI: 10.1016/j.cis.2015.08.008

[7] Abouzeid AZM, Fuerstenau DW. Flow of materials in rod mills as compared to ball mills in dry systems. International Journal of Mineral Processing. 2012;**102**:51-57. DOI: 10.1016/j.minpro.2011.09.013

[8] Heyes GW, Kelsall DF, Stewart PSB. Continuous grinding in a small wet rod mill part I. Comparison with a small ball mill. Powder Technology. 1973;**7**:319-325. DOI: 10.1016/0032-5910(73)80043-9

[9] Tavares LM, de Carvalho RM, Guerrero JC. Simulating the bond rod mill grindability test. Minerals Engineering. 2012;**26**:99-101. DOI: 10.1016/j.mineng.2011.10.015

[10] Cooper TG, de Leeuw NH. A computer modeling study of the competitive adsorption of water and organic surfactants at surfaces of the mineral scheelite. Langmuir. 2004;**20**:3984-3994. DOI: 10.1021/la049796w

[11] Oja M, Tuunila R. The influence of comminution method to particle shape. In: Massacci P, editor. Developments in Mineral Processing. Elsevier; 2000. p. C4-64-C64-70. DOI: 10.1016/S0167-4528(00)80028-9

[12] Moosakazemi F, Mohammadi MRT, Mohseni M, Karamoozian M, Zakeri M. Effect of design and operational parameters on particle morphology in ball mills. International Journal of Mineral Processing. 2017;**165**:41-49. DOI: 10.1016/j.minpro.2017.06.001

[13] Ulusoy U, Yekeler M. Correlation of the surface roughness of some industrial minerals with their wettability parameters. Chemical Engineering and Processing. 2005;**44**:557-565. DOI: 10.1016/j.cep.2004.08.001

[14] Vizcarra TG, Wightman EM, Johnson NW, Manlapig EV. The effect of breakage method on the shape properties of an iron-oxide hosted copper-gold ore. Minerals Engineering. 2011;**24**:1454-1458. DOI: 10.1016/j.mineng.2011.07.007

[15] Francioli D. Effect of operational variables on ball milling. Tijdschrift Voor Theologie. 2015;**52**:180-180

[16] Hicyilmaz C, Ulusoy U, Yekeler M. Effects of the shape properties of talc and quartz particles on the wettability based separation processes. Applied Surface Science. 2004;**233**: 204-212. DOI: 10.1016/j.apsusc..2004.03.209

[17] Yekeler M, Ulusoy U, Hicyilmaz C. Effect of particle shape and roughness of talc mineral ground by different mills on the wettability and floatability. Powder Technology. 2004; **140**:68-78. DOI: 10.1016/j.powtec.2003.12.012

[18] Ulusoy U, Hicyilmaz C, Yekeler M. Role of shape properties of calcite and barite particles on apparent hydrophobicity. Chemical Engineering and Processing. 2004;**43**:1047-1053. DOI: 10.1016/j.cep.2003.10.003

[19] Ulusoy U, Yekeler M, Hicyilmaz C. Determination of the shape, morphological and wettability properties of quartz and their correlations. Minerals Engineering. 2003;**16**: 951-964. DOI: 10.1016/j.mineng.2003.07.002

[20] Koh PTL, Hao FP, Smith LK, Chau TT, Bruckard WJ. The effect of particle shape and hydrophobicity in flotation. International Journal of Mineral Processing. 2009;**93**:128-134. DOI: 10.1016/j.minpro.2009.07.007

[21] Verrelli DI, Bruckard WJ, Koh PTL, Schwarz MP, Follink B. Particle shape effects in flotation. Part 1: Microscale experimental observations. Minerals Engineering. 2014;**58**: 80-89. DOI: 10.1016/j.mineng.2014.01.004

[22] Xia WC. Role of particle shape in the floatability of mineral particle: An overview of recent advances. Powder Technology. 2017;**317**:104-116. DOI: 10.1016/j.powtec.2017.04.050

[23] Feng D, Aldrich C. A comparison of the flotation of ore from the Merensky reef after wet and dry grinding. International Journal of Mineral Processing. 2000;**60**:115-129. DOI: 10.1016/S0301-7516(00)00010-7

[24] Zhu GL, Wang YH, Liu XW, Yu FS, Lu DF. The cleavage and surface properties of wet and dry ground spodumene and their flotation behavior. Applied Surface Science. 2015; **357**:333-339. DOI: 10.1016/j.apsusc.2015.08.257

[25] Xu LH, Hu YH, Wu HQ, Tian J, Liu J, Gao ZY, Wang L. Surface crystal chemistry of spodumene with different size fractions and implications for flotation. Separation and Purification Technology. 2016;**169**:33-42. DOI: 10.1016/j.seppur.2016.06.005

[26] Ilhan S, Kalpakli AO, Kahruman C, Yusufoglu I. The investigation of dissolution behavior of gangue materials during the dissolution of scheelite concentrate in oxalic acid solution. Hydrometallurgy. 2013;**136**:15-26. DOI: 10.1016/j.hydromet.2013.02.013

[27] Gao ZY, Bai D, Sun W, Cao XF, Hu YH. Selective flotation of scheelite from calcite and fluorite using a collector mixture. Minerals Engineering. 2015;**72**:23-26. DOI: 10.1016/j.mineng.2014.12.025

[28] Gao ZY, Sun W, Hu YH. New insights into the dodecylamine adsorption on scheelite and calcite: An adsorption model. Minerals Engineering. 2015;**79**:54-61. DOI: 10.1016/j.mineng.2015.05.011

[29] Cooper TG, de Leeuw NH. A combined ab initio and atomistic simulation study of the surface and interfacial structures and energies of hydrated scheelite: Introducing a CaWO4 potential model. Surface Science. 2003;**531**:159-176. DOI: 10.1016/S00039-6028(03)00362-5

[30] Deng LQ, Zhao G, Zhong H, Wang S, Liu GY. Investigation on the selectivity of N-((hydroxyamino)-alkyl) alkylamide surfactants for scheelite/calcite flotation separation. Journal of Industrial and Engineering Chemistry. 2016;**33**:131-141. DOI: 10.1016/j.jiec.2015.09.027

[31] Wang JJ, Gao ZY, Gao YS, Hu YH, Sun W. Flotation separation of scheelite from calcite using mixed cationic/anionic collectors. Minerals Engineering. 2016;**98**:261-263. DOI: 10.1016/j.mineng.2016.09.006

[32] Han HS, Hu YH, Sun W, Li XD, Cao CG, Liu RQ, Yue T, Meng XS, Guo YZ, Wang JJ, Gao ZY, Chen P, Huang WS, Liu J, Xie JW, Chen YL. Fatty acid flotation versus BHA flotation of tungsten minerals and their performance in flotation practice. International Journal of Mineral Processing. 2017;**159**:22-29. DOI: 10.1016/j.minpro.2016.12.006

[33] Yue T, Han HS, Hu YH, Sun W, Li XD, Liu RQ, Gao ZY, Wang L, Chen P, Zhang CY, Tian MJ. New insights into the role of Pb-BHA complexes in the flotation of tungsten minerals. Journal of Metals. 2017;**69**:2345-2351. DOI: 10.1007/s11837-017-2531-3

[34] Rupp F, Gittens RA, Scheideler L, Marmur A, Boyan BD, Schwartz Z, Geis-Gerstorfer J. A review on the wettability of dental implant surfaces I: Theoretical and experimental aspects. Acta Biomaterialia. 2014;**10**:2894-2906. DOI: 10.1016/j.actbio.2014.02.040

[35] Baek Y, Kang J, Theato P, Yoon J. Measuring hydrophilicity of RO membranes by contact angles via sessile drop and captive bubble method: A comparative study. Desalination. 2012;**303**:23-28. DOI: 10.1016/j.desal.2012.07.006

[36] Galet L, Patry S, Dodds J. Determination of the wettability of powders by the Washburn capillary rise method with bed preparation by a centrifugal packing technique. Journal of Colloid and Interface Science. 2010;**346**:470-475. DOI: 10.1016/j.jcis.2010.02.051

[37] Williams M, Fuerstenau D. A simple flotation method for rapidly assessing the hydrophobicity of coal particles. International Journal of Mineral Processing. 1987;**20**:153-157

[38] Yarar B, Kaoma J. Estimation of the critical surface tension of wetting of hydrophobic solids by flotation. Colloids and Surfaces. 1984;**11**:429-436

[39] Hu YH, Gao ZY, Sun W, Liu XW. Anisotropic surface energies and adsorption behaviors of scheelite crystal. Colloid Surface A. 2012;**415**:439-448. DOI: 10.1016/j.colsurfa.2012.09.038

[40] Gao ZY, Sun W, Hu YH. Mineral cleavage nature and surface energy: Anisotropic surface broken bonds consideration. Transactions of Nonferrous Metals Society of China. 2014;**24**:2930-2937. DOI: 10.1016/S1003-6326(14)63428-2

[41] Han HS, Liu WL, Hu YH, Sun W, Li XD. A novel flotation scheme: Selective flotation of tungsten minerals from calcium minerals using Pb-BHA complexes in Shizhuyuan. Rare Metals. 2017;**36**:533-540. DOI: 10.1007/s12598-017-0907-8

[42] Ulusoy U, Kursun I. Comparison of different 2D image analysis measurement techniques for the shape of talc particles produced by different media milling. Minerals Engineering. 2011;**24**:91-97. DOI: 10.1016/j.mineng.2010.05.011

[43] Ulusoy U, Yekeler M. Dynamic image analysis of calcite particles created by different mills. International Journal Of Mineral Processing. 2014;**133**:83-90. DOI: 10.1016/j.minpro.2014.10.006

[44] Morgan DJ, Jerram DA. On estimating crystal shape for crystal size distribution analysis. Journal of Volcanology and Geothermal Research. 2006;**154**:1-7. DOI: 10.1016/j.jvolgeores.2005.09.016

[45] Mock A, Jerram DA. Crystal size distributions (CSD) in three dimensions: Insights from the 3D reconstruction of a highly porphyritic rhyolite. Journal of Petrology. 2005;**46**:1525-1541. DOI: 10.1093/petrology/egi024

[46] Berger A, Herwegh M, Schwarz JO, Putlitz B. Quantitative analysis of crystal/grain sizes and their distributions in 2D and 3D. Journal of Structural Geology. 2011;**33**:1751-1763. DOI: 10.1016/j.jsg.2011.07.002

[47] Jerram DA, Mock A, Davis GR, Field M, Brown RJ. 3D crystal size distributions: A case study on quantifying olivine populations in kimberlites. Lithos. 2009;**112**:223-235. DOI: 10.1016/j.lithos.2009.05.042

[48] Gao ZY, Sun W, Hu YH, Liu XW. Surface energies and appearances of commonly exposed surfaces of scheelite crystal. Transactions of Nonferrous Metals Society of China. 2013;**23**:2147-2152. DOI: 10.1016/S1003-6326(13)62710-7

[49] Mogilevsky P, Parthasarathy TA, Petry MD. Anisotropy in room temperature microhardness and fracture of CaWo(4) scheelite. Acta Materialia. 2004;**52**:5529-5537. DOI: 10.1016/j.actamat.2004.08.022

[50] Mogilevsky P. Identification of slip systems in CaWO4 scheelite. Philosophical Magazine. 2005;**85**:3511-3539. DOI: 10.1080/14786430500227996

[51] Longo VM, Gracia L, Stroppa DG, Cavalcante LS, Orlandi M, Ramirez AJ, Leite ER, Andres J, Beltran A, Varela JA, Longo E. A joint experimental and theoretical study on the nanomorphology of $CaWO_4$ crystals. Journal of Physical Chemistry C. 2011;**115**: 20113-20119. DOI: 10.1021/jp205764s

[52] Li HL, Li TD, Liu HX, Huang BB, Zhang Q. Hierarchical flower-like nanostructures of anatase TiO_2 nanosheets dominated by {001} facets. Journal of Alloys and Compounds. 2016;**657**:1-7. DOI: 10.1016/j.jallcom.2015.09.257

[53] Gao ZY, Li CW, Sun W, Hu YH. Anisotropic surface properties of calcite: A consideration of surface broken bonds. Colloid Surface A. 2017;**520**:53-61. DOI: 10.1016/j.colsurfa.2017.01.061

[54] Gao Z, Hu Y, Sun W, Drelich JW. Surface-charge anisotropy of scheelite crystals. Langmuir. 2016;**32**:6282-6288. DOI: 10.1021/acs.langmuir.6b01252

[55] Cebeci Y, Sonmez I. A study on the relationship between critical surface tension of wetting and oil agglomeration recovery of calcite. Journal of Colloid and Interface Science. 2004;**273**:300-305. DOI: 10.1016/j.jcis.2004.01.032

[56] Gao YS, Gao ZY, Sun W, Hu YH. Selective flotation of scheelite from calcite: A novel reagent scheme. International Journal of Mineral Processing. 2016;**154**:10-15. DOI: 10.1016/j.minpro.2016.06.010